Published in final edited form as:
*Neuron*. 2023 November 15; 111(22): 3650–3667.e6. doi:10.1016/j.neuron.2023.08.008.

# Distinct Circuits in Anterior Cingulate Cortex Encode Safety Assessment and Mediate Flexibility of Fear Reactions

**Kaibin Wu**[1,2,3,4,5,9], **Dijia Wang**[1,2,3,4,5,9], **Yuwei Wang**[6,9], **Peiwen Tang**[1,2,3,4,5,9], **Xuan Li**[1], **Yidi Pan**[1], **Huizhong W. Tao**[7,8], **Li I. Zhang**[7,8], **Feixue Liang**[1,2,3,4,5,6,10,*]

[1]School of Biomedical Engineering, Southern Medical University, Guangzhou, 510515, China

[2]Guangdong-Hong Kong-Macao Greater Bay Area Center for Brain Science and Brain-Inspired Intelligence, Southern Medical University, Guangzhou, 510515, China

[3]Key Laboratory of Mental Health of the Ministry of Education, Southern Medical University, Guangzhou, 510515, China

[4]Department of Anaesthesiology, Zhujiang Hospital of Southern Medical University, Guangzhou, 510220, China

[5]Guangdong Province Key Laboratory of Psychiatric Disorders, Southern Medical University, Guangzhou, 510515, China

[6]Department of Psychology, School of Public Health, Southern Medical University, Guangzhou, 510515, China

[7]Center for Neural Circuits & Sensory Processing Disorders, Zilkha Neurogenetic Institute, Keck School of Medicine, University of Southern California, Los Angeles, CA 90033, USA

[8]Department of Physiology & Neuroscience, Keck School of Medicine, University of Southern California, Los Angeles, CA 90033, USA

[9]These authors contributed equally

[10]Lead contact

## Summary

Safety assessment and threat evaluation are crucial for animals to live and survive in the wilderness. However, neural circuits underlying safety assessment and its transformation to mediate flexibility of fear-induced defensive behaviors remain largely unknown. Here, we report that distinct neuronal populations in mouse anterior cingulate cortex (ACC) encode safety status by selectively responding under different contexts of auditory threats, with one preferably

---

[*] Correspondence: liangfx@smu.edu.cn.

**Author contributions:** F.L. conceived the study, supervised the project, and wrote the manuscript. K.W., D.W., Y.W., and P.T. performed the behavioral experiments and all the data analysis. X.L. performed the slice recording experiments. Y.P. performed the neural tracing and anatomical experiments. L.I.Z. and H.W.T. helped with discussion of the study and contributed to the writing of the manuscript.

Declaration of interests
The authors declare no competing interests.

Inclusion and diversity
We support inclusive, diverse, and equitable conduct of research.

activated when animal staying in a self-deemed safe zone, and another specifically activated in more dangerous environmental settings that led to escape behavior. The safety-responding neurons preferentially target the zona incerta (ZI), which suppresses the superior colliculus (SC) via its GABAergic projection, while the danger-responding neurons preferentially target and excite SC. These distinct corticofugal pathways antagonistically modulate SC responses to threat, resulting in context-dependent expression of fear reactions. Thus, ACC serves as a critical node to encode safety/danger assessment and mediate behavioral flexibility through differential top-down circuits.

## Introduction

Safety need is considered as a most fundamental motivation for animals' behaviors for them to live and survive in the wilderness. Animals constantly assess their safety status in a dynamically changing environment, and when encountering threats, are able to quickly choose an appropriate behavioral reaction (e.g. to escape from the source of threats and approach to a refuge) to evade harm [1–3]. The safety assessment is critically dependent on the animal's overall evaluation of environmental contexts, with prior experience and internal states also contributing to the perceived level of danger [4–11]. A proper judgement of the safety status allows the animal to choose to act by selecting the most effective and efficient strategy of action among many possibilities or to ignore the external threat stimuli [1,2]. Such flexibility is essential for increasing the ultimate survival chance. For example, in a relatively safe situation, suppression of defensive reactions to likely non-life-threatening events can minimize costs associated with unnecessary escape responses, thus optimizing fitness in the long run. Safety assessment is thus a critical factor for determining the flexibility of animals' behavioral reactions under environmental danger.

Despite the essential requirement of safety assessment, how it is effectuated in brain circuits to specifically guide behavioral reactions remains poorly understood. In particular, studies on neural bases for safety assessment in natural unlearned behaviors have remained scarce. We hypothesized that there exist safety assessment devoted circuits in higher-level cortical areas, which contain neurons with their activity correlated with the environmental safety situation, and that through a top-down modulation of lower-level brain regions for the execution of behavior, these neurons can affect whether and when fear reactions are expressed. A potential candidate is the medial prefrontal cortex (mPFC). This structure has been implicated in risk-based decision making [12–15]. It has also been shown to be involved in the expression and extinction of learned fear responses [10,16–18]. In addition, anatomical studies of the mPFC suggest that it can modulate many subcortical structures through its broad corticofugal projections [19,20]. However, whether specific neuronal populations in the mPFC can encode environmental safety related information is unknown.

Previous studies have established robust behavioral paradigms of sensory threat induced fear/defensive reactions [21–26]. These paradigms provide a foundation for understanding the regulatory circuits of fear/defensive behaviors [5,6,8,27,28]. In this study, by exploiting auditory threat induced fear/defensive behavior under paradigms of differentially-assessed environmental safety, we interrogated the neural circuits for how safety/danger context is encoded and interpreted. With micro-endoscopic imaging of $Ca^{2+}$ activity in freely moving mice, we found that subpopulations of neurons in a specific mPFC region, the anterior cingulate cortex (ACC), could selectively represent safety/danger contexts. Via differential corticofugal projections, these ACC neurons relayed safety- and danger-related information to the superior colliculus (SC) and antagonistically modulated the SC activity, which contributed to the flexibility of SC-dependent fear/defensive reactions under different contexts. Our results suggest that ACC can serve as a critical node to relay safety assessment information and to control behavioral flexibility upon environmental threats.

## Results

### Self-built nest is a self-deemed safe zone

When we investigated behaviors of freely moving mice in an enclosed arena separated into two connected chambers, we noticed that after the mouse became accustomed to the surrounding it begun to build a nest by collecting cotton balls scattered on the floor (Figure S1A). It usually took the mouse a few hours to build a nest (Figure S1B–S1C). The self-built nest was always located in a corner or along the wall (Figure 1A), which are considered safer zones in the arena [29]. After the nest building, the animal spent most of the time staying in the nest, longer than the time spent in corners when no nest was present (Figure 1B–1C). In addition, mice that had experienced auditory threats (see STAR Methods) built a nest faster than naïve animals (Figure 1D–1E). Furthermore, after experiencing auditory threats (Figure 1F), the animals initially staying in the nest exhibited less anxiety-like behaviors compared to those in the arena without a nest, as shown by elevated plus maze (EPM) (Figure 1G–1H) and open field (OF) tests (Figure 1I–1J), suggesting less fear experience. Thus, the self-built nest may be naturally deemed by the animal as a safe zone.

### Safety status determines fear reactions

To test how environmental safety status influences the behavioral response of the animal to threat signals, we placed the mouse in the arena and allowed it to complete the nest building. Auditory threat signals (broadband noise, 5 sec, 70 dB sound pressure level [SPL]) were then applied when the animal was in the chamber without the nest (scene 1) or when it was resting in the nest (scene 2) (Figure 1K) for at least 5 trials each scene in a randomized order (see STAR Methods). For a subset of mice, after the first set of tests, the self-built nest was replaced by an artificial (“sham”) nest and auditory stimulation was applied when the animal was outside (scene 3) or inside (scene 4) the sham nest in a randomized order (Figure 1K). We observed different behaviors under these different scenarios/contexts. For scene 1, the mouse quickly escaped into the nest (Figure 1L, first panel) with a fast running speed (Figure 1M, first panel), consistent with a defensive flight response under auditory threats [8,21,23,27,30]. For scene 2, however, the mouse mostly stayed in the nest during the auditory stimulation with no obvious freezing observed. Only occasionally it moved outside but then shortly returned to the nest (Figure 1L–1M, second panel). For scene 3, the mouse usually ran into the other chamber but rarely into the sham nest, and for scene 4, it usually ran out of the sham nest (Figure 1L–1M, right two panels). The quantifications of the total flight distance (Figure 1N), maximum running speed (Figure 1O) and probability of flight (Figure 1P) during the auditory stimulation indicate that escape behavior was nearly absent in scene 2 but strong in all the other three scenarios.

To provide a simplified quantification of the behavioral outcome, we scored the behavior with values 1-7 to indicate from the strongest to no defense phenotypes (Figure S2A–S2C). This “safety score” was on average much higher for scene 2 than the other three scenarios (Figure 1Q), indicating that the animals exhibited minimum or no escape response when staying in the self-built nest, while displaying strong escape in the other scenarios. No difference was found between male and female mice (Figure S2D–S2E). We next calculated a context selectivity index (CSI) by comparing the safety scores inside ($S_i$) and outside ($S_o$) the nest (self-built or sham) (see STAR Methods). The CSI in our test cohort was much higher for the self-built than sham nest (Figure 1R), indicating a strong context-dependency of the behavioral expression (i.e. very different reactions between inside- and outside-nest conditions). The CSI was close to 0 for the sham nest, indicating a very similar escape response regardless of whether the animal was inside or not. We also tested the dependency on the sound loudness. For scenes with the self-built nest, the louder the sound, the stronger was the escape response (i.e. lower safety score) in the outside-nest condition, whereas the animal consistently exhibited minimum escape response (i.e. high safety score) in the inside-nest condition (Figure 1S). The mean (± SD) latency of escape was 1.40 ± 0.95 sec after the noise onset and then it took 2.22 ± 1.71 sec for the animal to return to the nest at noise intensity of 70 dB SPL (Figure 1T). After returning to the nest, the animal stayed there for a much longer time than a spontaneous return before exposure to auditory threats (Figure S1D–S1E). For the trials starting with the animal staying in the nest, after exposure to auditory threats, the louder the noise, the longer the animal remained to stay in the nest (Figure S1F–S1G). Together, these data suggest that the observed differences in behavioral reactions upon the same auditory cue could be attributed to a difference in the perceived level of danger in different scenarios. The self-built (but not sham) nest provides the animal with a safe zone where the perceived level of danger is reduced. In other words, animals flexibly express fear reactions depending on their assessment of environmental safety.

## Safety- and danger-preferring neuronal populations in mPFC

Previously, mPFC has been implicated in the regulation of fear responses [10,17,31–34]. After exposing mice to auditory threats in the behavioral arena, we found significant neuronal activation in the mPFC region, revealed by c-Fos staining (see STAR Methods). Among the subdivisions of the mPFC, ACC contained the largest number of activated neurons (Figure 2A–2B). We thus focused on this area and examined whether it could play a role in the observed safety status-dependent regulation of escape behavior. We first investigated the dynamics of ACC neuronal activity in different scenarios using micro-endoscope (miniscope) recording of $Ca^{2+}$ signals [35] (Figure 2C). Threat-exposure-event-related neurons were identified through the receiver operating characteristic (ROC) analysis (see STAR Methods). Figure 2D shows three example cells, with cell 1 activity related to both inside- and outside-nest bouts, cell 2 to inside-nest bouts only and cell 3 to outside-nest bouts only (Figure 2E). We used auROC ≥ 0.65 as a criterion to identify neurons with their activity related to either inside- or outside-nest bouts (Figure 2F). In this population of neurons, we observed four types of cells, as shown by an example recording (Figure 2G). The first type exhibited a short-latency auditory-evoked response with similar amplitudes regardless of whether the animal was inside the self-built nest or not (Figure 2G, cell #1-2 on the left, also see Figure S3A–S3B, brown), suggesting that these neurons responded to auditory signals per se. Retrograde tracing confirmed that ACC received direct input from auditory sensory structures such as the auditory cortex and medial geniculate body (MGB) (Figure S3C–S3D). The second type showed a short-latency auditory-triggered response when inside but not outside the self-built nest (Figure 2G, cell #3-6, also see Figure S3A–S3B, green). In the outside-nest scenario, a large $Ca^{2+}$ increase was observed in these neurons around the time when the animal returned to the nest. The third type exhibited little response when inside the nest, but in the outside-nest scenario a strong $Ca^{2+}$ response was observed, which more-or-less temporally correlated with the onset of flight (Figure 2G, cell #9-12, also see Figure S3A–S3B, red). The fourth type appeared to combine the response properties of the second and third types, exhibiting a short-latency response when inside the self-built nest and a delayed response in the outside-nest scenario (Figure 2D, cell #7-8, also see Figure S3A–S3B, blue). The responses of these neurons were quite consistent across trials (Figure 2G, right panel).

To better illustrate the event-related activity at the population level, we used an interpolation method (Figure S3E–S3J) to align the $Ca^{2+}$ responses of different neurons based on event onsets such as the onset of flight and that of nest-entering. For non-auditory-only (type 2-4) neurons, we ranked them based on the relative response levels in two different contexts (Figure S3A) and computed a safety-fear selectivity index (SFSI; see STAR Methods) from the peak amplitudes of $Ca^{2+}$ responses in the inside-nest ($P_i$) and outside-nest ($P_o$, before returning to the nest) conditions. Based on the SFSI, we could separate them into three categories: danger-responding, safety-responding and neutral (Figure 2H). The population average of $\Delta F/F$ showed that the danger-responding cells (Figure 2I, red) did not respond to the auditory stimulation when inside the self-built nest but exhibited a strong response around the time of flight (latency = 1.15 ± 0.29 sec, Figure S3B) in the outside-nest scenario. On the contrary, the safety-responding cells (Figure 2I, green) responded quickly to the onset of auditory stimulation when inside the self-built nest. They did not do so when outside the self-built nest, but exhibited a strong response around the time when the animal returned to the nest (also see Figure S3B). The neutral cells (Figure 2I, blue) resembled the danger-responding cells in the outside-nest scenario but the safety-responding cells in the inside-nest scenario. Overall, there were comparable numbers of safety-responding (19.1%) and danger-responding (14.6%) neurons in ACC, while auditory-only and neutral cells were fewer (Figure 2J). In the safety-responding population, about two-thirds (63.8%) exhibited a robust response at the time of returning to the nest (Figure 2J, dark green curve).

We focused on the two ACC subpopulations exhibiting selectivity to the safety/danger context. We examined their activity dynamics under other scenarios. The safety-responding neurons exhibited very different dynamics in the sham-nest than self-built-nest scenario in that they did not respond to the auditory stimulation when inside the sham nest (Figure 3A–3B). In addition, while most of them responded to nest-returning, this response was absent if no nest was present (Figure 3C–3D). The danger-responding neurons exhibited a similar response around the time of flight when both outside the self-built nest and inside the sham nest (Figure 3E–3F), implying similarly fearful situations. Their responses around the time of flight could not be explained by running per se, since their activity was uncorrelated with the speed of spontaneous locomotion (Figure 3G–3H). These results further suggest that the responses of safety- and danger-responding neurons correlate well with the perceived safety/danger status.

To more quantitatively illustrate the difference in activity dynamics between the safety- and danger-responding subpopulations, we reduced dimensionality and projected the time-evolving average population activity in the space of the first two principal components (Figure 3I–3J, left panels). The distance between the two trajectories greatly increased following the onset of flight or noise stimulation (Figure 3I–3J, right panel), demonstrating that these the two cell populations behaved very differently upon auditory threats. Next, we trained a linear decoder, a binary classifier based on a support vector machine (SVM) learning algorithm [36], to discriminate behaviors in two different scenarios (scene 1 and scene 2) based on the imaged activity of the safety- or danger-responding subpopulation (see STAR Methods). In either case, the accuracy of the decoder was significantly higher than that on shuffled data (Figure 3K), demonstrating a strong correlation between the activity dynamics of safety/danger-responding ACC neurons and the safety/danger context. Further consistent with this notion, after the termination of auditory stimulation (“post-threat” period, 5 sec), the activity level of safety-responding cells was significantly higher than danger-responding cells in both outside- and inside-nest scenarios, although they did not differ during the resting period just before the auditory stimulation (Figure 3L–3M).

## Distinct corticofugal pathways from ACC

The presence of safety- and danger-responding neurons suggests that ACC may modulate fear responses through the context-dependent activity of these neurons. To further explore this issue, it is important to understand where these neurons project to. We thus investigated the ACC targets by injecting AAV-Syn-GFP into ACC (Figure 4A–4B). We found that ACC axons strongly targeted the basolateral amygdala (BLA), dorsomedial striatum (DMS), zona incerta (ZI), superior colliculus (SC) and dorsal periaqueductal gray (dPAG) (Figure 4C). The latter two structures, especially the SC, are known to be involved in threat-induced flight behavior [6,21,37,38]. By performing fiber photometry recording of ACC axon terminals in these different target areas (see STAR Methods), we found that the ACC→BLA projection did not respond under the auditory threat (Figure 4D). The ACC→DMS projection showed sound-triggered $Ca^{2+}$ responses that were invariant in response amplitude between different contexts (Figure 4E), suggesting that this pathway may relay auditory-only information. The ACC projections to ZI and SC, however, exhibited context-selective responses resembling safety- and danger-responding neurons, respectively (Figure 4F–4G): the projection to ZI had a much stronger response to the onset of auditory stimulation when inside than outside the self-built nest and had a distinct delayed response when the animal returned to the nest from outside, whereas that to SC exhibited a much stronger response to the auditory stimulation when outside than inside the nest (Figure 4H). These results suggest that the ACC→ZI projection may mainly transmit safety-related information, while the ACC→SC projection may relay danger-related information.

Next, we labeled ACC neurons targeting ZI and SC by injecting a retrograde dye (CTB) of different colors into ZI and SC, respectively (Figure 4I). In the mPFC region, retrogradely labeled neurons were mainly found in ACC relative to other subdivisions (Figure S4). In

ACC, cells retrogradely labeled from ZI and SC injections exhibited differential laminar profiles (Figure 4J–4K), and the co-labeled cells overall only accounted for a small fraction of the total labeled neurons (Figure 4L). We then specifically imaged $Ca^{2+}$ responses of individual ACC neurons projecting to ZI or SC, using an intersectional viral labeling approach and miniscope recording (Figure 4M and 4P). Both safety- and danger-responding cells were observed in the ZI- and SC-projecting ACC populations (Figure 4N and 4Q). However, the proportions of the two cell types were different: danger-responding cells dominated over safety-responding cells in the SC-projecting population (danger/safety: 2.45), while safety-responding cells dominated in the ZI-projecting population (safety/danger: 3.64) (Figure 4O and 4R). The population average of $\Delta F/F$ signals of cell bodies revealed response properties consistent with the terminal imaging results, with the SC-projecting population exhibiting higher danger-related activity and the ZI-projecting population higher safety-related activity (Figure 4S and 4U). Finally, we compared the SFSI of the target-defined subpopulation with the general ACC population (Figure 4T and 4V). The distribution of SFSIs was relatively symmetrical for the general ACC population, with two peaks around −1 and 1. However, distributions for the SC- and ZI-projecting subpopulations were skewed, with a bias towards negative (fear-dominating) and positive (safety-dominating) values, respectively. These data together suggest that ACC neurons projecting to ZI and SC are largely separate subpopulations, and that danger- and safety-responding ACC neurons preferentially target SC and ZI, respectively.

## Integration of ACC safety/danger-related signals in SC

Previous studies have shown that SC plays an essential role in mediating defensive flight induced by visual or auditory cues[21,37,38, 39,66,67]. The anatomical data further suggest that ACC may modulate SC activity through a direct projection to SC and an indirect pathway via ZI, which projects to SC with an inhibitory output [8,27,40]. To confirm these pathways, we expressed fluorescence proteins of different colors in ACC and ZI, respectively. The labeled ACC and ZI axons terminate in overlapping areas in the midbrain, in particular the deep layers of SC and dPAG (Figure 5A). Next, we expressed ChR2 in ACC or ZI axons and performed whole-cell recording from SC neurons in slice preparations (Figure 5B). The results confirmed that SC neurons received direct excitatory and inhibitory synaptic inputs from ACC and ZI, respectively (Figure 5C–5D). Furthermore, whole-cell recording from ZI neurons retrogradely labeled from SC confirmed that SC-projecting ZI neurons received direct excitatory input from ACC (Figure 5E–5H). Therefore, our data indicate a direct excitatory and an indirect inhibitory pathway from ACC to SC, which presumably have opposite effects on SC activity.

Using dual-color fiber photometry, we imaged simultaneously the ensemble $Ca^{2+}$ activity of ACC→SC and ZI→SC axon terminals, which expressed GCaMP7 and jRGECO1a, respectively (Figure 5I). The ACC→SC terminals exhibited a much stronger auditory-triggered response than the ZI→SC terminals in the outside-nest scenario, and vice versa for the inside-nest scenario (Figure 5J–5L). In addition, the ZI→SC terminals exhibited a delayed response when the animal returned to the nest (Figure 5J, red). These inverse response dynamics suggest that the two corticofugal pathways from ACC (ACC→SC, ACC→ZI→SC) may modulate SC activity in an antagonistic manner.

We next investigated how SC activity varied under different contexts and whether it correlated with different behavioral responses, by performing miniscope recording of $Ca^{2+}$ signals in deep layers of SC (Figure 5M). As shown by an example recording (Figure 5N) and the population summary (Figure 5O–5P), auditory noise induced $Ca^{2+}$ responses of large amplitudes in SC neurons in the outside- but not inside-nest scenario. Therefore, the low and high levels of SC activity correlate with the absence and presence of fear response, respectively. We postulated that by modulating SC activity, ACC outputs via direct and indirect pathways could regulate the escape response in a context-dependent manner.

## Antagonistic modulation of fear reactions by ACC-mediated pathways

To test the above hypothesis, we applied Designer Receptors Exclusively Activated by Designer Drugs (DREADD)-based chemogenetics for activity manipulations. Excitatory (hM3Dq) and inhibitory (hM4Di) DREADD receptors were expressed in desired cells for activation and inactivation, respectively. Slice whole-cell recording confirmed the effectiveness of the ligand CNO in increasing or suppressing spiking activity (Figure S5A–S5B). We first tested the effect of SC activation/inactivation on the context-dependent escape response (Figure 6A). Activation of SC increased escape in the inside-nest scenario but without affecting it in the outside-nest scenario, resulting in a reduction of CSI (Figure 6B–6C, Figure S6A–S6B). On the other hand, inactivation of SC reduced escape in the outside-nest scenario but without any effect in the inside-nest scenario, which also resulted in a reduction of CSI (Figure 6D–6E, Figure S6C–S6D).

We next investigated whether manipulating any modulatory input to SC could generate a similar effect to manipulating SC *per se*. We expressed hM3Dq or hM4Di in ACC or ZI and locally infused CNO into a specific target area to upregulate or downregulate activity of a desired pathway (Figure 6F, 6K, 6P). The context-dependent escape behavior was markedly affected. Activating the ACC→SC pathway increased escape in the inside-nest scenario and greatly reduced the CSI (Figure 6G–6H, Figure S6E–S6F), whereas inactivating this pathway reduced escape in the outside-nest scenario, which also resulted in a significant reduction of the CSI (Figure 6I–6J, Figure S6G–S6H). Manipulating ACC→ZI or ZI→SC pathway produced an opposite effect: activating either of these pathways reduced escape in the outside-nest scenario (Figure 6L–6M, 6Q–6R), whereas inactivation increased escape in the inside-nest scenario (Figure 6N–6O, 6S–6T). In all cases, the CSI was reduced (Figure S6I–S6P). Our results suggest that activity of the ACC→SC pathway promotes while that of the ACC→ZI→SC pathway suppresses escape response. This supports an antagonistic relationship between these two ACC-mediated corticofugal pathways to SC.

Consistent with the notion that activation of the ACC→SC pathway enhances fear response, we found that activation of this pathway also increased anxiety-like behaviors, as shown by the results of EPM and OF tests (Figure S5C–S5G, S5M–S5O). On the other hand, inactivation of ACC→ZI axon terminals did not significantly affect anxiety-like behaviors (Figure S5H–S5L, S5P–S5R), suggesting that inactivation of the ACC→ZI projection may not be sufficient for changing the baseline anxiety level.

### ACC projections to SC and dPAG have similar functional effects

ACC innervates both the deep layers of SC and its adjacent dPAG region (Figure 4C). Since fiber photometry recording of the ensemble $Ca^{2+}$ activity of Vglut2+ neurons in dPAG revealed a similar context dependency (Figure S7), we could not exclude the possibility that the ACC→dPAG projection also contributed to the observed effects in the above experiments. To further distinguish SC vs. dPAG contributions, we employed anterograde transsynaptic tagging with a double-injection strategy [38,41] to restrict opsin expression within ACC-recipient SC or dPAG neurons (Figure 7A, 7G). For optogenetic activation, we chose a weak light intensity that itself did not induce running (Figure 7B, 7H). We observed similar modulatory effects by activation/inactivation of either ACC-recipient SC or ACC-recipient dPAG neurons on the defensive behavior (Figure 7C–7F, 7I–7L). These results suggest that ACC projections to SC and dPAG may have a similar functional role in the context-dependent fear response.

### Auditory sensory inputs to SC are not modulated by the safety/danger context

Besides ACC, the SC/dPAG region also receives salient excitatory inputs from auditory sensory structures such as the auditory cortex (ACx) and inferior colliculus (IC) [23,30,40,42]. Both structures can convey auditory threat signals, but whether these inputs could also be modulated by the safety/danger context and contribute to the behavioral flexibility has been unknown (Figure 8A). To address this issue, we expressed GCaMP in the cortex of IC (ICx), which provides auditory input to SC/dPAG [23,40]. Photometry recording of the ensemble $Ca^{2+}$ signal of ICx terminals in SC revealed similar auditory-triggered responses in different contexts (Figure 8B–8E). We also expressed GCaMP in SC-projecting ACx neurons, using a retrograde viral injection strategy (Figure 8F). Miniscope recording again revealed that auditory stimulation triggered similar $Ca^{2+}$ responses in inside- and outside-nest scenarios (Figure 8G–8I). These results indicate that auditory sensory inputs to SC are not specifically modulated by the safety/danger context.

## Discussion

In this study, we have shown that animals exhibit flexible behavioral reactions under different safety/danger contexts. With single-cell and projection-based $Ca^{2+}$ imaging in freely moving animals and projection-specific activity manipulations, we demonstrated that ACC is critically involved in context-dependent adaptive fear/defensive behavior by bidirectionally modulating the activity of SC, which is important for driving the escape response.

### Flexible auditory threat-induced fear reactions

We found that the auditory threat induced defensive behavior is flexible and context-dependent. When the animal is initially in a self-deemed safe zone, defensive behavior upon a potentially threatening event is greatly suppressed, possibly because in this circumstance the event is unlikely life-threatening. Suppressing nonessential flight then reduces energy cost, which is beneficial to the animal in the long run. We have not observed any difference in such context-dependent defensive behavior between male and female mice (Figure S2D–S2E), in line with a recent study on visually evoked defensive behavior [43]. In addition, the study reports that the estrus phase does not significantly affect the visually induced defense behavior in females [43], likely reflecting a most fundamental need of animals for safety across the lifespan. Nevertheless, since the estrous cycle is associated with fluctuations of ovarian hormone levels and the latter can potentially affect the brain state, we do not exclude the possibility that the estrous phase may be able to modulate the auditory-evoked defensive behavior in some ways or to some extent. This intriguing question requires more extensive investigations in the future.

## The functional role of ACC and its functional cell types

Previous studies of ACC have demonstrated its diverse roles in pain-related affect and high-level cognitive processes, including attention allocation, decision making, learning, cost-benefit calculation, as well as conflict and error monitoring [44–53]. This structure is well positioned to modulate widely distributed networks through top-down projections to many areas of the brain [54–58], and thus is thought to broadly regulate behaviors. Here in this study, our results have elucidated a less recognized functional role of ACC in assessing environmental safety.

Our imaging data have revealed that ACC contains functionally heterogeneous neuronal subgroups. As implicated by the auditory-only cells, ACC receives auditory information that is independent of safety/danger contexts, likely directly from the auditory cortex and auditory thalamus (Figure S3C–S3D). Context-specific neurons, however, are present. The danger-responding cells do not respond to auditory threat signals when the animal stays in a safe zone, its self-built nest, and behaviorally the animal ignores the threat signals. These cells on the other hand respond in various danger scenarios, not immediately to sensory stimulation, but with a delay (Figure S3B). Their responses temporally correspond to the onset of flight, but cannot be explained by locomotion *per se*. These responses may thus reflect an escape decision after appraising the situation and calculating the escape strategy. The safety-responding cells respond almost immediately to the threat signals when the animal stays in the self-built nest, possibly because the brain has already been preset to operate in a “safe” mode. Most of these neurons also exhibit robust activation when the animal returns to the nest from flight, which is absent if the nest is absent from the arena. Our data thus suggest a strong correlation between the activity of danger-/safety-responding cells and the danger/safety context. Indeed, based on the observed activity of either of these two cell populations, a linear classifier can discriminate danger/safety contexts with high accuracies (Figure 3K). Together, our results suggest that these context-specific ACC subpopulations can encode information of safety assessment. It is worth noting that the activity pattern of ACC neurons forms a continuum, containing a middle fraction of neurons which more-or-less combine the response properties of danger- and safety-responding cells (i.e. neutral cells). Their activity may contribute to the population coding of safety/danger contexts in a graded manner, or alternatively their activity might be irrelevant to safety assessment. The functional significance of neutral cells remains to be investigated in the future. The ACC could either receive context-specific information from other structures, or alternatively the context-dependent activity could emerge in ACC by integrating multi-dimensional information, e.g. from sensory cortices [19,58–61] and the hippocampal formation

[62–64]. It will be of great interest to investigate in the future which scenario is true and how context-specific activity emerges in brain circuits.

## Bidirectional modulation of SC activity by distinct ACC corticofugal circuits

Previous studies on the neural circuits regulating SC-mediated unlearned fear/defensive behaviors have been mostly focused on subcortical areas [5,6,8,27,28]. The impact of ACC revealed in this study suggests more extensive neural networks underlying the flexibility of fear/defensive reactions. The direct projections of ACC neurons to SC and ZI are consistent with previous reports [58,65,66]. SC- and ZI-projecting ACC neurons appear to be largely separate cell populations as examined functionally and anatomically (Figure 4). Our slice recording data confirmed that the ACC→SC projection excites SC neurons, whereas the ACC→ZI→SC pathway disynaptically inhibits SC neurons via ACC-recipient ZI neurons (Figure 5A–5H). Thus, through these functionally antagonistic ACC-mediated corticofugal pathways, ACC can bidirectionally regulate the SC activity. The projection-based imaging of the ensemble $Ca^{2+}$ activity indicated that the ACC→SC pathway relays primarily danger-related information, while the ACC→ZI→SC pathway relays predominantly safety-related information (Figure 5I–5L). These sources of information converge in SC, modulating SC responses to auditory signals which are otherwise context-invariant (Figure 8B-8I). Projection-specific activity manipulations demonstrated that enhancing and suppressing the activity of the ACC→SC pathway promotes and suppresses the escape response, respectively, and vice versa for the ACC→ZI→SC pathway (Figure 6). A similar mechanism likely operates in dPAG as well, since the ACC→dPAG pathway also promotes the escape response (Figure 7G–7L) and ZI also projects to dPAG[8,27,42]. Thus, through its safety- and danger-responding neuronal populations and their associated corticofugal pathways towards SC, the ACC critically contributes to safety/danger-context-dependent flexible fear/defensive behavior. Whether this functional role of ACC generalizes to other sensory modalities is an intriguing question that remains to be studied. Since previous studies have demonstrated that SC neurons in the intermediate layer, where ACC and ZI axons project to, mediate visual looming induced defensive behaviors [24,67,68], we postulate that ACC corticofugal projections can play a similar role in modulating visually evoked defensive behaviors.

## A working model

Previously, it has been suggested that evidence of threat is integrated in SC and passes through a synaptic threshold at the level of dPAG to initiate escape [69]. Based on our results in the current study, we propose that SC/dPAG neurons can integrate external threat signals and safety assessment information from ACC. As such, SC/dPAG interprets ACC’s evaluation of environmental safety according to the relative strengths of the opposing signals relayed from the two ACC-mediated corticofugal pathways (Figure 8J). Only when the summed signal exceeds a certain threshold, can the output of SC/dPAG initiate escape actions. Otherwise, no escape is initiated. Importantly, the safety-responding ACC neurons respond quickly to the sound onset when the animal stays inside the self-built nest. This would result in a fast inhibitory input to SC via ZI, ensuring the timely suppression of SC neuronal responses to the sound signals and thus the fear response. In danger scenarios, the delayed response of the danger-responding ACC neurons, when transmitted to SC, may facilitate the temporal summation of SC synaptic inputs in dPAG [21], thus promoting the initiation of escape.

Altogether, our study suggests that ACC can serve as an important node to encode safety assessment and to mediate the flexibility of defensive behavioral responses according to the overall environmental safety situation. This would allow the animal to effectively and efficiently adapt to different challenges in a dynamic environment. The context-dependent top-down control of fear responses by ACC raises the possibility that dysregulation of ACC circuits may contribute to fear-related emotional disorders such as phobias and post-traumatic stress disorder [70].

## STAR★ METHODS

### RESOURCE AVAILABILITY

**Lead contact—**Further information and requests for resources and reagents should be directed to and will be fulfilled by the lead contact, Feixue Liang (Liangfx@smu.edu.cn).

**Materials availability—**This study did not generate new, unique reagents.

#### Data and code availability

- All data reported in this paper will be shared by the lead contact upon request.
- All original code has been deposited at Zenodo and is publicly available as of the date of publication. DOIs are listed in the key resources table.
- Any additional information required to reanalyze the data reported in this paper is available upon request.

### EXPERIMENTAL MODEL AND STUDY PARTICIPANT DETAILS

All experimental procedures were approved by the Animal Care and Use Committee at the Southern Medical University. Male and female wild-type C57BL/6J and transgenic Vglut2-Cre (JAX# Stock No. 028863.), Thy1-Cre (JAX# Stock No. 006143) and Gad2-Cre (JAX# Stock No. 028867) mice were used in this study. All transgenic mice were first purchased from Jackson Laboratories and backcrossed to C57BL/6J to generate a breeding colony. Animals used for stereotaxic surgery were aged 9–12 weeks. Animals were housed under a 12 h light–dark cycle, with food and water available ad libitum. The housing facility had a temperature of 21–23 °C and a humidity of 40–60%. Flying saucer pet wheels were placed in the home cages for environmental enrichment.

### METHOD DETAILS

**Viruses and tracers—**The following adeno-associated viruses (AAVs) and tracers were used in this study. For micro-endoscopic calcium imaging and fiber photometry recording experiments, AAV2/9-syn-jGCaMP7s-WPRE ($9.83\times10^{12}$ v.g./ml, OBiO), AAV2/1-syn-FLEX-jGCaMP7s-WPRE ($1.58\times10^{13}$ v.g./ml, OBiO), AAV2/9-hSyn-FLEX-NES-jRGECO1a-WPRE ($9.2\times10^{12}$ v.g./ml, OBiO) and AAV2-retro-hSyn-Cre (1×1013 v.g./ml, Vigene) were used. For chemogenetic experiments, AAV2/9-hSyn-hM4D(Gi)-

mCherry-WPRE ($3.5\times10^{12}$ v.g./ml, OBiO) and AAV2/9-hSyn-hM3D(Gq)-mCherry ($3.5\times10^{12}$ v.g./ml, OBiO) were used. For optogenetic experiments, AAV2/1-hSyn-Cre ($5.3\times10^{13}$ v.g./ml, BrainVTA), AAV2/9-EF1α-DIO-eYFP ($3.5\times10^{12}$ v.g./ml, OBiO), AAV2/9-DIO-hChR2 (H134R)-eYFP ($6.5 \times 10^{12}$ v.g./ml, OBiO), AAV2/9-DIO-GtACR1-eYFP ($5.0 \times 10^{12}$ v.g./ml, OBiO), AAV2/9-CaMKIIα-hChR2(H134R)-eYFP ($6.83\times10^{12}$ v.g./ml, OBiO) were used. For anterograde tracing, AAV2/9-syn-FLEX-eYFP ($9.83\times10^{12}$ v.g./ml, OBiO) and AAV2/9-hSyn-GFP ($5.14\times10^{12}$ v.g./ml, BrainVTA) were used. For retrograde tracing, Cholera Toxin subunit B (CTB 488, 555, 0.25%; Invitrogen) was used. For *ex vivo* electrophysiology, AAV2/9-CaMKIIα-hChR2(H134R)-eYFP ($6.83\times10^{12}$ v.g./ml, OBiO), AAV2/9-EF1α-DIO-mCherry-WPRE-hGH ($5.35\times10^{12}$ v.g./ml, BrainVTA), AAV2/9-DIO-hChR2(H134R)-eYFP ($6.5 \times 10^{12}$ v.g./ml, OBiO) were used. AAVs were diluted with clean PBS on the day before injection if the original viral titer was too high.

## Surgical procedures and virus injections

**General virus/tracer injections:** Mice were anaesthetized with isoflurane (1.25%–2% in 0.7–1.5 l/min of $O_2$) and mounted on a stereotaxic device. The skin was cleaned and Betadine and lidocaine (2%, ~0.3 ml) was injected for local anesthesia. A craniotomy was made over the desired brain region. The AAVs (encoding GCaMP7s, hM4D(Gi), hM3D(Gq), ChR2, GFP or mCherry) or tracer (CTB 488/555) were used, depending on the purpose of the experiments and the strain of mice. A beveled glass micropipette (tip diameter, 30-40 μm; pulled with the Model P-97, Sutter Instrument) was used to deliver the virus or tracer, through pressure injection with a microsyringe pump (World Precision Instruments) at a rate of 20 nl/min. After injection, pipette stayed for 10 min before being withdrawn. 0.1 mg/kg buprenorphine was injected subcutaneously after the surgery and the animal was returned to the home cage. Recovery time was at least 2 weeks before cannula or optic fiber implantation, behavioral testing or recording experiments. After the experiments, brain was extracted, sectioned and imaged under a confocal microscope to confirm viral expression.

**Surgeries for micro-endoscopic calcium imaging:** The surgical procedures were generally performed following previous studies [71,72,73]. To image neurons in the deep layers of SC, AAV1-syn-GCaMP7s-WPRE (200-300 nl) was injected unilaterally into SC (ML 0.6, AP −4.05 from bregma, DV −1.65 mm) of C57BL/6J mouse. To image neurons in the deep layers of ACC, AAV2/1-syn-FLEX-GCaMP7s-WPRE (100-200 nl) was injected unilaterally into ACC (ML 0.4, AP +1.38 from bregma, DV −1.8 mm) of the Thy1-Cre mouse. To image projection-specific neurons in the auditory cortex (SC-projecting ACx neurons) or ACC (SC- or ZI-projecting ACC neurons), AAV2-retro-hSyn-Cre was firstly injected unilaterally into SC or ZI (ML 0.98, AP −1.4 from bregma, DV −4.55 mm). Two weeks after the first injection, AAV2/1-syn-FLEX-GCaMP7s-WPRE was then injected unilaterally into AC or ACC. 20-30 minutes after the second virus injection, a gradient refractive index (GRIN) lens (1.0 mm diameter and 4.2 mm length for SC recording; 1.0 mm diameter and 4.2mm length for ACC recording; 0.5 mm diameter and 6.00 mm length for ACx recording; Inscopix) was then implanted above the injection site and secured to the skull using super glue as well as dental cement. Mice were given a subcutaneous injection of Ketoprofen (4 mg/kg) during surgery. Ibuprofen was administered through drinking water (30 mg/kg), lasting for 4 days for postoperative care. After a recovery period of 1-4 weeks, the micro-endoscope together with a titanium baseplate were placed above the lens. The position of the micro-endoscope was adjusted till the cells and the blood vessels appeared sharp in the focal plane. Then, the baseplate was secured at the position with dental cement. All mice were handled and habituated for over 3 days before imaging experiments.

**Surgeries for fiber photometry recording:** AAV encoding GCaMP7s (100-200 nl) was injected unilaterally into dPAG (for recording dPAG neuronal $Ca^{2+}$ signals, ML 0.45 mm, AP −4.5 mm from bregma, DV −2.15mm), ICx (for recording ICx axon terminals; ML −1.50 mm, AP −5.10 mm from bregma, DV −1.30 mm), ACx (ML −3.90 mm, AP −2.80 mm from bregma, DV −2.15 mm), ZI (ML −0.98 mm, AP −1.34 mm from bregma, DV −4.55 mm) or ACC (ML −0.45 mm, AP +1.35 mm from bregma, DV −2.00 mm). For dual-color optical fiber photometry recording, AAV2/9-hSyn-FLEX-NES-jRGECO1a-WPRE and AAV1-syn-GCaMP7s-WPRE were injected unilaterally into ZI and ACC of Gad2-Cre mouse, respectively. 2~3 weeks after the virus injection, a ferrule fiber-optic cannula (200 μm core diameter, 0.39 numerical aperture; RWD) was implanted above the target region (for recording from BLA, ML 3.05 mm, AP −1.25 mm from bregma, DV −4.45 mm; for recording from DMS, ML 1.70 mm, AP 0.50 mm from bregma, DV 2.45 mm; for recording from dPAG, ML −0.80 mm, AP −4.50 mm from bregma, DV −2.30 mm) and secured to the skull using dental cement.

**Surgeries for chemogenetic activation and inhibition:** AAV2/9-hSyn-hM4D(Gi)-mCherry-WPRE or AAV2/9-hSyn-hM3D(Gq)-mCherry-WPRE (150-200 nl) was injected bilaterally into ACC (for ACC→ZI or ACC→SC pathway manipulations) or ZI (for ZI→SC pathway manipulations). 2~3 weeks after the virus injection, drug cannulas (140 μm internal diameter; RWD) were bilaterally implanted into the ZI or SC and secured with dental cement.

**Surgeries for optogenetic activation and inhibition:** For optogenetic activation of the ACC→ZI or ACC→SC pathway, AAV2/9-CaMKIIα-hChR2(H134R)-eYFP or eYFP only (200 nl) was injected bilaterally into ACC. 2~3 weeks after the virus injection, optical fibers (200 μm core diameter; RWD) were bilaterally implanted above the ZI or SC and secured with dental cement. For optogenetic activation or inhibition of ACC-recipient neurons in SC or dPAG, a two-step injection method was used. AAV1-hSyn-Cre (200 nl) was firstly injected into ACC. 5-7 days after the first injection, AAV2/9-EF1α-DIO-eYFP (100 nl, for activation), AAV2/9-EF1α-DIO-GtACR1-eYFP (100 nl, for inhibition) or AAV2/9-EF1α-DIO-eYFP (100 nl, for control) was then selectively injected into either SC or dPAG. 20 minutes after the final injection, optical fibers (200 μm core diameter; RWD) were bilaterally implanted above the SC or dPAG and secured with dental cement.

## Behavioral testing

### General flow of behavioral testing

***Nest-building.:*** Behavioral testing was performed in a test arena divided into two chambers (dimensions of each chamber in cm: 35 w, 75 l, 55 h), similar to what was previously used [23]. There was an opening connecting the two chambers, which allowed the animal to move freely back and forth. A speaker was attached to each chamber for sound stimulation and two cameras were placed on the top and one side of the arena respectively to monitor the locomotion of the animal. Before a new animal was placed in, the behavioral arena was cleaned with 10% alcohol. Bedding materials, nesting materials, food and water were also replaced. A day before behavioral testing, the mouse was individually introduced in the behavioral arena. 2-4 hours after explorations, most mice would begin to build a nest in a corner or near a wall and it would take a few hours to complete the nest-building (Figure S1A–S1C). After that the mouse would consider the self-built nest as a safe context, thus resting inside the nest for most of the time. They only occasionally explored outside the nest (Figure 1B–1C). Only after a mouse successfully completed nest building, it was advanced to behavioral testing.

***Context-dependent behavioral testing.:*** To test context-dependent fear responses upon auditory threats, we tested two scenarios for all the mice. In the first scenario, auditory threat (a 5 sec-duration noise sound at 70 dB SPL) was applied when the mouse was resting in the nest (inside-nest bouts, scene 1); while in the second scenario, the same auditory threat was applied when mouse was exploring outside the nest (outside-nest bouts, scene 2) (Figure 1K). A typical behavioral testing session included 5-8 inside-nest bouts and 5-8 outside-nest bouts tested in a randomized order. The interval between auditory threats was > 2 min. In a subset of mice, after the first set of tests, the self-built nest was replaced by a sham nest and a second set of behavioral testing was performed, which included 5-8 inside-sham-nest bouts and 5-8 outside-sham-nest bouts in a randomized sequence. A behavioral testing session was performed per animal per day, with at most 2 repetitions per animal. The location and speed of the mouse during behavioral testing was monitored in real-time with two cameras for off-line analysis.

**Behavioral scoring.:** The mouse behavior was video recorded at 25 fps. The location and moving trajectories were analyzed off-line with a commercial software (Smart 3.0, Panlab). We assigned a safety score from 1 to 7 based on the mouse's maximum flight speed and ending location (Figure S2A–S2C). We quantitatively measured several parameters of the behavior, including total travel distance, maximum locomotion speed and defense probability (percentage of trials with a safety score < 6) (Figure 1N–1P). A context selectivity index (CSI) was calculated as: $CSI = (Si - So)/(So + Si)$, where Si and So were safety scores for inside- and outside-nest bouts, respectively. CSI close to 1 indicates strong context-dependency with strong safety responses in inside-nest bouts, while CSI = 0 indicates no context-dependency.

**Elevated plus maze (EPM) and open field (OF) tests.:** EPM and OF tests were performed 10 min after exposing the mouse to auditory threats, following the methods used in a previous study [74]. EPM was performed within a white Plexiglass apparatus with two closed arms and two opened arms, elevated 30 cm above the ground. The animal was placed in the center of the crossed maze, and its locomotion was recorded with a video camera for 5 min. The percentage of time spent in the open arms was determined by offline analysis. For OF test, the mouse was placed at the center of a cubic box (60 cm long, 60 cm wide, 35 cm high), and locomotor activity was monitored for 10 min. The percentage of time spent in the center area was analyzed offline.

**Chemogenetic manipulations during behavior:** Mice expressing hM4D(Gi) or hM3D(Gq) were given a local infusion of CNO (5 μM, 120 nl) or solvent at a rate of 100 nl/min through the implanted cannula to the target region, 30 min before behavioral testing. The behavioral testing was similar to described above, except that the number of bouts in each session was slightly smaller (3-5 trials for both inside-nest and outside-nest conditions).

**Optogenetic manipulations during behavior:** For optogenetic activation, blue laser pulses (20 Hz, 25 ms pulse duration, 5 sec stimulation duration) were delivered to the target region using a laser stimulator (Aurora 400, Newdoon). For the activation of SC (Figure 7B) or PAG (Figure 7H) neurons, the laser intensity was first tested and the maximum intensity that did not directly elicit escape behavior was selected for experiments. For terminal activation, laser intensity of 5 mw was used. Laser pulses were continuously applied during each trial. For the place preference test (Figure S5M–S5R), the two chambers were randomly designated as the laser-on and laser-off chamber. Laser pulses were applied when the mouse entered the laser-on chamber and continued until the animal exited that chamber [74].

**Micro-endoscopic calcium imaging—**A micro-endoscope (UCLA Miniscope V4, purchased from Open Ephys; https://github.com/Aharoni-Lab/Miniscope-DAQ-QT-Software) was used to image GCaMP7s-expressing neurons in SC, ACx or ACC in freely-moving conditions. One week before behavioral testing, a custom-made object with the same weight as the micro-endoscope was fixed on the head of the subject mouse for it to adapt to weight-bearing running. After that, no significant difference of mouse behavior was observed under auditory threats between weight-bearing and non-bearing conditions. During each trial of behavioral testing, $Ca^{2+}$ fluorescence signals and behavior were simultaneously video recorded, at 25 fps for 30 sec duration, initiated by an external trigger signal synchronized with the onset of noise stimulation. To better distinguish event-related neurons, only the inside-nest bouts with safety score equal to 7 and outside-nest bouts with safety score equal to 1 were selected for further analysis. In general, data from 3-5 inside-nest bouts and outside-nest bouts were selected for analysis from each behavioral testing session. The micro-endoscope was neither unloaded nor refocused in a behavioral testing session, as to ensure the same field of view (FOV) over time. All the selected $Ca^{2+}$ fluorescence videos were firstly concatenated and motion-corrected using the NormCorre algorithm (https://github.com/flatironinstitute/NoRMCorre)(Pnevmatikakis and Giovannucci, 2017). Individual neurons were identified with Constrained Non-Negative Matrix Factorization (CNMF-E; https://github.com/zhoupc/CNMF_E) (Cunningham and Yu, 2014; Zhou et al., 2018) and a raw $Ca^{2+}$ activity trace was obtained for each neuron by averaging all the pixel values in the associated region of interest (ROI). Next, fluorescence changes (ΔF/F) were calculated and z-scored. Finally, extracted ROIs as well as their traces were manually inspected to exclude false-positive neurons, and the motion-corrected $Ca^{2+}$ fluorescence video was also manually inspected to add missing neurons.

**Fiber photometry recording—**The photometry recording experiment was performed using a fiber photometry system (Thinker Biotech, Nanjing). Before each recording experiment, we adjusted the light intensity of fiber optic patch cables to be 40-60 μW. After each recording trial, we turned off the laser immediately to avoid photo bleaching. The $Ca^{2+}$ signal was then exported to MATLAB for off-line analysis. The value of fluorescence change (ΔF/F) was calculated by $(F - F0)/F0$, where F0 was the baseline fluorescence. We also performed a time normalization for the $Ca^{2+}$ signal in outside-nest bouts from fiber photometry recording, similar to the method used for $Ca^{2+}$ signal from micro-endoscopic calcium imaging recoding.

**Slice preparation and recording—**C57BL/6J mice injected with ChR2 virus in ACC or ZI, Ai14 mice injected with ChR2 virus in ACC and retrograde Cre virus in SC, or C57BL/6J mice injected with hM4D(Gi) or hM3D(Gq) virus in ACC were used for slice recording. Following the urethane anesthesia, the mouse was decapitated and the brain was rapidly removed and immersed in an ice-cold dissension buffer (composition: 60 mM NaCl, 3 mM KCl, 1.25 mM $NaH_2PO_4$, 25 mM $NaHCO_3$, 115 mM sucrose, 10 mM glucose, 7 mM $MgCl_2$, 0.5 mM $CaCl_2$; saturated with 95% $O_2$ and 5% $CO_2$; pH¼7.4). Brain slices of 350 μm thickness containing the target regions (SC, ZI or ACC, depending on the purpose of recording) were cut in a coronal plane using a vibrating microtome (Leica VT1000s). Slices were allowed to recover for 30 min in a submersion chamber filled with the warmed (35 °C) ACSF and then to cool gradually to the room temperature until recording. The spatial expression pattern of ChR2-eYFP or tdTomato in each slice was examined under a fluorescence microscope before recording. Only slices with the correct location for expression were used for further recording. Cells were visualized with IR-DIC and fluorescence microscopy (Olympus BX51 WI) for specific target neurons. Glass patch pipettes with 4–5MΩ impedance were used for whole-cell recording. Internal solution contained: 130 mM K-gluconate, 4 mM KCl, 2 mM NaCl, 10 mM HEPES, 0.2 mM EGTA, 4 mM ATP, 0.3 mM GTP and 14 mM phosphocreatine (pH, 7.25; 290 mOsm). Signals were recorded with an Axopatch 700B amplifier (Molecular Devices) under voltage-clamp mode at a holding voltage of −70 mV and +10 mV for excitatory and inhibitory currents, respectively. The recoded current was filtered at 2 kHz and sampled at 10 kHz. A blue light pulse of 5-ms duration was applied to active ChR2-expressing axon terminals. To confirm the functional connection of ACC→ZI or ACC→SC/ZI→SC pathways, 1mM TTX and 1mM 4-aminopyridine was added to the external solution to record monosynaptic responses. To verify the effect of hM4D(Gi) or hM3D(Gq), spikes of hM4D(Gi) or hM3D(Gq) expressing neurons in ACC were recorded before and after perfusion of CNO (5 μM) and after washing out CNO.

**Sound generation—**Software for sound stimulation was custom made in LabVIEW (National Instruments). Sound was generated by the sound wave generation module and delivered through a calibrated open acoustic delivery system using a TDT ES1 speakers (Tucker-Davis Technologies), as previously described [77]. For behavioral testing on different scenarios, a 5 sec noise at 70 dB SPL was delivered selectively from the speaker at the side of the mouse's location side manually. The outside- and inside-nest bouts were performed depending on both the mouse's location and state, while they were alternated as much as possible. In both outside- and inside-nest bouts, noise stimulation was applied only when the mouse was quiet for more than 3s, and the inter-stimulus interval was no less than 2 minutes to avoid behavioral adaptation. In a small subset of experiments, we also tested dependency on sound intensity by using pre-calibrated noise from 40 to 80 dB SPL.

**Immunohistochemistry and cell quantification—**For detecting c-Fos expression, viral expression and grin lens location, frozen sections were prepared. Animals were deeply anesthetized and perfused with 50 mL of PBS, followed by 50 mL of ice-cold 4% paraformaldehyde (PFA, Sigma). After perfusion, brain was harvested, soaked in 20% of sucrose in PBS for 48 hours and then embedded with O.C.T compound (Fisher Healthcare). 40 μm thick coronal sections were collected with a cryostat (RWD, FS800). Brain sections were then washed with PBS (10 min for 3 times) and PBST (0.1% Triton X-100 in PBS, 10 min for 3 times), blocked in 10% normal goat serum (NGS, Beyotime) in PBST for 40 minutes under room temperature, and then incubated with primary antibodies in 3% NGS in PBST overnight at 4°C. Sections were then washed with PBST (10 min for 3 times), incubated in the secondary antibodies in 1% NGS in PBST for 2h under room temperature, then washed with PBST (10 min for 3 times). The sections were finally mounted onto microscope slides and covered with coverslips along with an anti-fade reagent containing DAPI (P36931, Invitrogen).

The primary antibody used was: rabbit monoclonal anti-c-fos (dilution 1:200, 2,250; Cell Signaling). The secondary antibody was: Alexa Fluor 488 goat anti-rabbit IgG (dilution 1:500, ab150077, Abcam).

The sections were photographed and analyzed using a confocal microscope. For each brain, all the images were taken with the exact same settings. Confocal images were acquired and cell counting was performed using ImageJ.

## QUANTIFICATION AND STATISTICAL ANALYSIS

### Analysis of event-related neurons

**Analysis of behavioral events:** To define event-related neurons, the accurate timing of behavioral events, such as flight onset and nest-entering onset, was first manually marked frame-by-frame from behavioral videos. The flight onset latency and nest-entering latency were then calculated as the time lag between the noise onset (determined by the timing of the trigger signal) and flight onset, and between flight onset and nest-entering onset, respectively (Figure 1T). We then synchronized the timing of behavioral events and $Ca^{2+}$ activity traces for further analysis.

**Analysis of event-related neurons in SC and AC:** The activity of individual cells during outside-nest bouts (aligned to the flight onset) and inside-nest bouts (aligned to the noise onset) was averaged across all corresponding trials within each imaged session and z-scored. Event-related neurons were defined by $Ca^{2+}$ activity during auditory threat presentation that was higher than the average baseline activity by 3 standard deviations. Average baseline activity was calculated over a 5 sec time window before the flight onset (for outside-nest bouts) or noise onset (for inside-nest bouts).

**Analysis of event-related neurons in ACC:** We used the receiver operating characteristic (ROC) analysis to identify whether neurons significantly responded during inside-nest bouts and/or outside-nest bouts. The true-positive rate and false-positive rate of the calcium signal of individual cell were calculated to generate ROC curves of both inside- and outside-nest bouts, and the area under the ROC curve was then calculated to generate auROCi and auROCo, which measured how strong the neural activity was related to inside- and outside-nest bouts, respectively (Figure 2D–2E). When either auROCi or auROCo was equal to or greater than 0.65, the neuron was considered as an event-related neuron (Figure 2F).

In the event-related neuronal population, a small subset exhibited a short-latency auditory-evoked response, which had a similar amplitude regardless of whether the animal was inside or outside the self-built nest (Figure 2G, cell #1-2, also see Figure S3A–S3B). Therefore, this small subset was defined as the auditory-only neuron (type 1) and the rest were defined as non-auditory-only (type 2-4) neurons. To quantify the average response during inside-nest bouts, the $Ca^{2+}$ activity traces of individual cells were aligned to the noise onset and averaged across all trials within an imaging session. To better quantify the average response of multiple behavioral events (flight or nest-entering) during outside-nest bouts, we performed a time normalization for the $Ca^{2+}$ activity trace of each trial, since the nest-entering latency was varied across trials (Figure 1T). Specifically, the $Ca^{2+}$ activity traces from the flight onset to nest-entering onset was first interpolated as a 2 sec signal and the rest of the signals remained unchanged (Figure S3E–S3J). Then the interpolated $Ca^{2+}$ activity traces of individual cells were aligned to the flight onset and averaged across all outside-nest bouts within an imaging session. After that, the averaged $Ca^{2+}$ activity trace was normalized to the largest peak amplitude during 0-1.5 sec after the flight onset (for outside-nest bouts) or noise onset (for inside-nest bouts).

**Safety-fear selectivity index (SFSI):** SFSI was calculated as: SFSI = (Po −Pi) / (Po + Pi), where Pi and Po were the peak amplitudes of the normalized $Ca^{2+}$ activity during inside- and outside-nest bouts, respectively. SFSI was used to classify non-auditory-only neurons into safety-responding neurons (SFSI ≥ 0.33), danger-responding neurons (SFSI ≤ −0.33) and neutral cells (−0.33 < SFSI < 0.33) (Figure 2H).

**Analysis of population dynamics during behavior and behavioral decoding:** To examine the separation of population responses between safety- and danger-responding cells for both scenarios, we performed principal components analysis (PCA, Matlab toolbox) [75,76] on the normalized $Ca^{2+}$ activity traces from each behavioral testing session. We first smoothed each trace (9 sec, 25 fps, total 225 frames) with a 20-frames smoothing window. For a given behavioral testing session which had m danger-responding cells and n safety-responding cells, we acquired a $m \times 225$ danger-responding cellular matrix and a $n \times 225$ safety-responding cellular matrix for outside- and inside-nest bouts, respectively. Next, we performed PCA to reduce the dimensionality of both danger-responding cellular matrix and safety-responding cellular matrix and projected them onto the first two principal components for visualization, respectively. Shown as an example session in the left panel of Figure 3I–3J, the trajectories between safety-responding cells and danger-responding cells indicated a strong separation for both outside- (Figure 3I, left) and inside-nest bouts (Figure 3J, left).

To further quantify the separation dynamics between safety- and danger-responding cell activity, we calculated Mahalanobis distance [76] between two trajectories during behavior, and averaged all data across behavioral testing sessions for both outside- (Figure 3I, right) and inside-nest bouts (Figure 3J, right).

To further analyze the relationship of animal behavior and population activity in ACC, a linear binary SVM decoder was trained to predict behavioral responses upon auditory threats under different scenarios with $Ca^{2+}$ activity of both safety- and danger-responding cells. A data matrix combining a binary behavior table with a $Ca^{2+}$ activity array was first established as the dataset of the decoder. The binary behavior table was established by labeling outside-nest bouts as 1 and inside-nest bouts as 0. The $Ca^{2+}$ activity array was established with a $N \times M \times T$ dimension matrix, where N is the number of safety- and danger-responding cells, M is the number of trials and T is the number of frames. The $Ca^{2+}$ activity trace of each cell was smoothed with a 15-frame smoothing window and normalized by the maximum value. 80% of cells were used to train a SVM decoder, while the $Ca^{2+}$ activity trace of outside-nest bouts or inside-nest bouts of the remaining cells were used to predict behavioral responses under different scenarios, respectively (10 fold cross-validation, sklearn in Python). To generate shuffled data as control, we randomly permuted the binary behavior table and performed the same decoding. To estimate the performance of the decoder, decoding was repeated 100 times and the cumulative distribution function (CDF) of accuracy was calculated (Figure 3K), similar to previously described [36].

**Statistics—**Shapiro–Wilk test was first applied to examine whether samples had a normal distribution. In the case of a normal distribution, t-test or analysis of variance test was applied. Otherwise, a non-parametric test (Wilcoxon signed-rank test in this study) was applied. Data were presented as Mean ±SEM, if not otherwise specified.

## Supplementary Material

Refer to Web version on PubMed Central for supplementary material.

## Acknowledgments

This work was supported by grants to F.L. from the National Natural Science Foundation of China (32271061), the Natural Science Funds for Distinguished Young Scholar of Guangdong province (2019B151502033), the STI2030-major projects (2021ZD0202600), and Guangzhou Science and Technology Plan Project (202206060004).

## References

1. Yilmaz M, and Meister M (2013). Rapid innate defensive responses of mice to looming visual stimuli. Curr Biol 23, 2011–2015. 10.1016/j.cub.2013.08.015. [PubMed: 24120636]
2. Branco T, and Redgrave P (2020). The Neural Basis of Escape Behavior in Vertebrates. Annu Rev Neurosci 43, 417–439. 10.1146/annurev-neuro-100219-122527. [PubMed: 32259462]
3. Jr C, and Blumstein D (2015). Escaping From Predators: An Integrative View of Escape Decisions 10.1017/CBO9781107447189.
4. Lenzi SC, Cossell L, Grainger B, Olesen SF, Branco T, and Margrie TW (2022). Threat history controls flexible escape behavior in mice. Curr Biol 32, 2972–2979 e2973. 10.1016/j.cub.2022.05.022. [PubMed: 35659863]

5. Salay LD, and Huberman AD (2021). Divergent outputs of the ventral lateral geniculate nucleus mediate visually evoked defensive behaviors. Cell Rep 37, 109792. 10.1016/j.celrep.2021.109792. [PubMed: 34610302]
6. Fratzl A, Koltchev AM, Vissers N, Tan YL, Marques-Smith A, Stempel AV, Branco T, and Hofer SB (2021). Flexible inhibitory control of visually evoked defensive behavior by the ventral lateral geniculate nucleus. Neuron 109, 3810–3822 e3819. 10.1016/j.neuron.2021.09.003. [PubMed: 34614420]
7. Wang X, Chou XL, Zhang LI, and Tao HW (2020). Zona Incerta: An Integrative Node for Global Behavioral Modulation. Trends Neurosci 43, 82–87. 10.1016/j.tins.2019.11.007. [PubMed: 31864676]
8. Chou XL, Wang X, Zhang ZG, Shen L, Zingg B, Huang J, Zhong W, Mesik L, Zhang LI, and Tao HW (2018). Inhibitory gain modulation of defense behaviors by zona incerta. Nat Commun 9, 1151. 10.1038/s41467-018-03581-6. [PubMed: 29559622]
9. Kunwar PS, Zelikowsky M, Remedios R, Cai H, Yilmaz M, Meister M, and Anderson DJ (2015). Ventromedial hypothalamic neurons control a defensive emotion state. Elife 4. 10.7554/eLife.06633.
10. Sotres-Bayon F, and Quirk GJ (2010). Prefrontal control of fear: more than just extinction. Curr Opin Neurobiol 20, 231–235. 10.1016/j.conb.2010.02.005. [PubMed: 20303254]
11. Salay LD, Ishiko N, and Huberman AD (2018). A midline thalamic circuit determines reactions to visual threat. Nature 557, 183–189. 10.1038/s41586-018-0078-2. [PubMed: 29720647]
12. Euston DR, Gruber AJ, and McNaughton BL (2012). The role of medial prefrontal cortex in memory and decision making. Neuron 76, 1057–1070. 10.1016/j.neuron.2012.12.002. [PubMed: 23259943]
13. Jentsch JD, Woods JA, Groman SM, and Seu E (2010). Behavioral characteristics and neural mechanisms mediating performance in a rodent version of the Balloon Analog Risk Task. Neuropsychopharmacology 35, 1797–1806. 10.1038/npp.2010.47. [PubMed: 20375994]
14. St Onge JR, Abhari H, and Floresco SB (2011). Dissociable contributions by prefrontal D1 and D2 receptors to risk-based decision making. J Neurosci 31, 8625–8633. 10.1523/JNEUROSCI.1020-11.2011. [PubMed: 21653866]
15. Tashjian SM, Wise T, and Mobbs D (2022). Model-based prioritization for acquiring protection. PLoS Comput Biol 18, e1010805. 10.1371/journal.pcbi.1010805. [PubMed: 36534704]
16. Alexandra Kredlow M, Fenster RJ, Laurent ES, Ressler KJ, and Phelps EA (2022). Prefrontal cortex, amygdala, and threat processing: implications for PTSD. Neuropsychopharmacology 47, 247–259. 10.1038/s41386-021-01155-7. [PubMed: 34545196]
17. Giustino TF, and Maren S (2015). The Role of the Medial Prefrontal Cortex in the Conditioning and Extinction of Fear. Front Behav Neurosci 9, 298. 10.3389/fnbeh.2015.00298. [PubMed: 26617500]
18. Marek R, Strobel C, Bredy TW, and Sah P (2013). The amygdala and medial prefrontal cortex: partners in the fear circuit. J Physiol 591, 2381–2391. 10.1113/jphysiol.2012.248575. [PubMed: 23420655]
19. Oh SW, Harris JA, Ng L, Winslow B, Cain N, Mihalas S, Wang Q, Lau C, Kuan L, Henry AM, et al. (2014). A mesoscale connectome of the mouse brain. Nature 508, 207–214. 10.1038/nature13186. [PubMed: 24695228]
20. Anastasiades PG, and Carter AG (2021). Circuit organization of the rodent medial prefrontal cortex. Trends Neurosci 44, 550–563. 10.1016/j.tins.2021.03.006. [PubMed: 33972100]
21. Evans DA, Stempel AV, Vale R, Ruehle S, Lefler Y, and Branco T (2018). A synaptic threshold mechanism for computing escape decisions. Nature 558, 590–594. 10.1038/s41586-018-0244-6. [PubMed: 29925954]
22. Fadok JP, Krabbe S, Markovic M, Courtin J, Xu C, Massi L, Botta P, Bylund K, Muller C, Kovacevic A, et al. (2017). A competitive inhibitory circuit for selection of active and passive fear responses. Nature 542, 96–100. 10.1038/nature21047. [PubMed: 28117439]
23. Xiong XR, Liang F, Zingg B, Ji XY, Ibrahim LA, Tao HW, and Zhang LI (2015). Auditory cortex controls sound-driven innate defense behaviour through corticofugal projections to inferior colliculus. Nat Commun 6, 7224. 10.1038/ncomms8224. [PubMed: 26068082]

24. Wei P, Liu N, Zhang Z, Liu X, Tang Y, He X, Wu B, Zhou Z, Liu Y, Li J, et al. (2015). Processing of visually evoked innate fear by a non-canonical thalamic pathway. Nat Commun 6, 6756. 10.1038/ncomms7756. [PubMed: 25854147]
25. Wang L, Chen IZ, and Lin D (2015). Collateral pathways from the ventromedial hypothalamus mediate defensive behaviors. Neuron 85, 1344–1358. 10.1016/j.neuron.2014.12.025. [PubMed: 25754823]
26. Shang C, Liu Z, Chen Z, Shi Y, Wang Q, Liu S, Li D, and Cao P (2015). BRAIN CIRCUITS. A parvalbumin-positive excitatory visual pathway to trigger fear responses in mice. Science 348, 1472–1477. 10.1126/science.aaa8694. [PubMed: 26113723]
27. Wang X, Chou X, Peng B, Shen L, Huang JJ, Zhang LI, and Tao HW (2019). A cross-modality enhancement of defensive flight via parvalbumin neurons in zona incerta. Elife 8. 10.7554/eLife.42728.
28. Hormigo S, Zhou J, and Castro-Alamancos MA (2020). Zona Incerta GABAergic Output Controls a Signaled Locomotor Action in the Midbrain Tegmentum. eNeuro 7. 10.1523/ENEURO.0390-19.2020.
29. Godsil BP, and Fanselow MS (2004). Light stimulus change evokes an activity response in the rat. Learn Behav 32, 299–310. 10.3758/bf03196029. [PubMed: 15672825]
30. Li Z, Wei JX, Zhang GW, Huang JJ, Zingg B, Wang X, Tao HW, and Zhang LI (2021). Corticostriatal control of defense behavior in mice induced by auditory looming cues. Nat Commun 12, 1040. 10.1038/s41467-021-21248-7. [PubMed: 33589613]
31. Rozeske RR, Jercog D, Karalis N, Chaudun F, Khoder S, Girard D, Winke N, and Herry C (2018). Prefrontal-Periaqueductal Gray-Projecting Neurons Mediate Context Fear Discrimination. Neuron 97, 898–910 e896. 10.1016/j.neuron.2017.12.044. [PubMed: 29398355]
32. Grunfeld IS, and Likhtik E (2018). Mixed selectivity encoding and action selection in the prefrontal cortex during threat assessment. Curr Opin Neurobiol 49, 108–115. 10.1016/j.conb.2018.01.008. [PubMed: 29454957]
33. Dejean C, Courtin J, Karalis N, Chaudun F, Wurtz H, Bienvenu TC, and Herry C (2016). Prefrontal neuronal assemblies temporally control fear behaviour. Nature 535, 420–424. 10.1038/nature18630. [PubMed: 27409809]
34. Courtin J, Chaudun F, Rozeske RR, Karalis N, Gonzalez-Campo C, Wurtz H, Abdi A, Baufreton J, Bienvenu TC, and Herry C (2014). Prefrontal parvalbumin interneurons shape neuronal activity to drive fear expression. Nature 505, 92–96. 10.1038/nature12755. [PubMed: 24256726]
35. Kingsbury L, Huang S, Wang J, Gu K, Golshani P, Wu YE, and Hong W (2019). Correlated Neural Activity and Encoding of Behavior across Brains of Socially Interacting Animals. Cell 178, 429–446 e416. 10.1016/j.cell.2019.05.022. [PubMed: 31230711]
36. Grant RI, Doncheck EM, Vollmer KM, Winston KT, Romanova EV, Siegler PN, Holman H, Bowen CW, and Otis JM (2021). Specialized coding patterns among dorsomedial prefrontal neuronal ensembles predict conditioned reward seeking. Elife 10. 10.7554/eLife.65764.
37. Shang C, Chen Z, Liu A, Li Y, Zhang J, Qu B, Yan F, Zhang Y, Liu W, Liu Z, et al. (2018). Divergent midbrain circuits orchestrate escape and freezing responses to looming stimuli in mice. Nat Commun 9, 1232. 10.1038/s41467-018-03580-7. [PubMed: 29581428]
38. Zingg B, Chou XL, Zhang ZG, Mesik L, Liang F, Tao HW, and Zhang LI (2017). AAV-Mediated Anterograde Transsynaptic Tagging: Mapping Corticocollicular Input-Defined Neural Pathways for Defense Behaviors. Neuron 93, 33–47. 10.1016/j.neuron.2016.11.045. [PubMed: 27989459]
39. Liang F, Xiong XR, Zingg B, Ji XY, Zhang LI, and Tao HW (2015). Sensory Cortical Control of a Visually Induced Arrest Behavior via Corticotectal Projections. Neuron 86, 755–767. 10.1016/j.neuron.2015.03.048. [PubMed: 25913860]
40. Benavidez NL, Bienkowski MS, Zhu M, Garcia LH, Fayzullina M, Gao L, Bowman I, Gou L, Khanjani N, Cotter KR, et al. (2021). Organization of the inputs and outputs of the mouse superior colliculus. Nat Commun 12, 4004. 10.1038/s41467-021-24241-2. [PubMed: 34183678]
41. Zingg B, Peng B, Huang J, Tao HW, and Zhang LI (2020). Synaptic Specificity and Application of Anterograde Transsynaptic AAV for Probing Neural Circuitry. J Neurosci 40, 3250–3267. 10.1523/JNEUROSCI.2158-19.2020. [PubMed: 32198185]

42. Wang H, Chen J, Xu X, Sun WJ, Chen X, Zhao F, Luo MH, Liu C, Guo Y, Xie W, et al. (2019). Direct auditory cortical input to the lateral periaqueductal gray controls sound-driven defensive behavior. PLoS Biol 17, e3000417. 10.1371/journal.pbio.3000417. [PubMed: 31469831]
43. Liu X, Feng X, Huang H, Huang K, Xu Y, Ye S, Tseng YT, Wei P, Wang L, and Wang F (2022). Male and female mice display consistent lifelong ability to address potential life-threatening cues using different post-threat coping strategies. BMC Biol 20, 281. 10.1186/s12915-022-01486-x. [PubMed: 36522765]
44. Holroyd CB, and Yeung N (2012). Motivation of extended behaviors by anterior cingulate cortex. Trends Cogn Sci 16, 122–128. 10.1016/j.tics.2011.12.008. [PubMed: 22226543]
45. Silvetti M, Seurinck R, and Verguts T (2013). Value and prediction error estimation account for volatility effects in ACC: a model-based fMRI study. Cortex 49, 1627–1635. 10.1016/j.cortex.2012.05.008. [PubMed: 22717205]
46. Laubach M, Caetano MS, and Narayanan NS (2015). Mistakes were made: neural mechanisms for the adaptive control of action initiation by the medial prefrontal cortex. J Physiol Paris 109, 104–117. 10.1016/j.jphysparis.2014.12.001. [PubMed: 25636373]
47. Kolling N, Wittmann MK, Behrens TE, Boorman ED, Mars RB, and Rushworth MF (2016). Value, search, persistence and model updating in anterior cingulate cortex. Nat Neurosci 19, 1280–1285. 10.1038/nn.4382. [PubMed: 27669988]
48. Shackman AJ, Salomons TV, Slagter HA, Fox AS, Winter JJ, and Davidson RJ (2011). The integration of negative affect, pain and cognitive control in the cingulate cortex. Nat Rev Neurosci 12, 154–167. 10.1038/nrn2994. [PubMed: 21331082]
49. Shenhav A, Botvinick MM, and Cohen JD (2013). The expected value of control: an integrative theory of anterior cingulate cortex function. Neuron 79, 217–240. 10.1016/j.neuron.2013.07.007. [PubMed: 23889930]
50. Ullsperger M, Danielmeier C, and Jocham G (2014). Neurophysiology of performance monitoring and adaptive behavior. Physiol Rev 94, 35–79. 10.1152/physrev.00041.2012. [PubMed: 24382883]
51. Birdsong WT, Jongbloets BC, Engeln KA, Wang D, Scherrer G, and Mao T (2019). Synapse-specific opioid modulation of thalamo-cortico-striatal circuits. Elife 8. 10.7554/eLife.45146.
52. Heilbronner SR, and Hayden BY (2016). Dorsal Anterior Cingulate Cortex: A Bottom-Up View. Annu Rev Neurosci 39, 149–170. 10.1146/annurev-neuro-070815-013952. [PubMed: 27090954]
53. Monosov IE, Haber SN, Leuthardt EC, and Jezzini A (2020). Anterior Cingulate Cortex and the Control of Dynamic Behavior in Primates. Curr Biol 30, R1442–R1454. 10.1016/j.cub.2020.10.009. [PubMed: 33290716]
54. Fiser A, Mahringer D, Oyibo HK, Petersen AV, Leinweber M, and Keller GB (2016). Experience-dependent spatial expectations in mouse visual cortex. Nat Neurosci 19, 1658–1664. 10.1038/nn.4385. [PubMed: 27618309]
55. Hu F, Kamigaki T, Zhang Z, Zhang S, Dan U, and Dan Y (2019). Prefrontal Corticotectal Neurons Enhance Visual Processing through the Superior Colliculus and Pulvinar Thalamus. Neuron 104, 1141–1152 e1144. 10.1016/j.neuron.2019.09.019. [PubMed: 31668485]
56. Leinweber M, Ward DR, Sobczak JM, Attinger A, and Keller GB (2017). A Sensorimotor Circuit in Mouse Cortex for Visual Flow Predictions. Neuron 96, 1204. 10.1016/j.neuron.2017.11.009.
57. Rajasethupathy P, Sankaran S, Marshel JH, Kim CK, Ferenczi E, Lee SY, Berndt A, Ramakrishnan C, Jaffe A, Lo M, et al. (2015). Projections from neocortex mediate top-down control of memory retrieval. Nature 526, 653–659. 10.1038/nature15389. [PubMed: 26436451]
58. Zhang S, Xu M, Chang WC, Ma C, Hoang Do JP, Jeong D, Lei T, Fan JL, and Dan Y (2016). Organization of long-range inputs and outputs of frontal cortex for top-down control. Nat Neurosci 19, 1733–1742. 10.1038/nn.4417. [PubMed: 27749828]
59. Han Y, Kebschull JM, Campbell RAA, Cowan D, Imhof F, Zador AM, and Mrsic-Flogel TD (2018). The logic of single-cell projections from visual cortex. Nature 556, 51–56. 10.1038/nature26159. [PubMed: 29590093]
60. Wang Q, Sporns O, and Burkhalter A (2012). Network analysis of corticocortical connections reveals ventral and dorsal processing streams in mouse visual cortex. J Neurosci 32, 4386–4399. 10.1523/JNEUROSCI.6063-11.2012. [PubMed: 22457489]

61. Zingg B, Hintiryan H, Gou L, Song MY, Bay M, Bienkowski MS, Foster NN, Yamashita S, Bowman I, Toga AW, and Dong HW (2014). Neural networks of the mouse neocortex. Cell 156, 1096–1111. 10.1016/j.cell.2014.02.023. [PubMed: 24581503]

62. Ongur D, and Price JL (2000). The organization of networks within the orbital and medial prefrontal cortex of rats, monkeys and humans. Cereb Cortex 10, 206–219. 10.1093/cercor/10.3.206. [PubMed: 10731217]

63. Cenquizca LA, and Swanson LW (2007). Spatial organization of direct hippocampal field CA1 axonal projections to the rest of the cerebral cortex. Brain Res Rev 56, 1–26. 10.1016/j.brainresrev.2007.05.002. [PubMed: 17559940]

64. Jay TM, and Witter MP (1991). Distribution of hippocampal CA1 and subicular efferents in the prefrontal cortex of the rat studied by means of anterograde transport of Phaseolus vulgaris-leucoagglutinin. J Comp Neurol 313, 574–586. 10.1002/cne.903130404. [PubMed: 1783682]

65. Hu TT, Wang RR, Du Y, Guo F, Wu YX, Wang Y, Wang S, Li XY, Zhang SH, and Chen Z (2019). Activation of the Intrinsic Pain Inhibitory Circuit from the Midcingulate Cg2 to Zona Incerta Alleviates Neuropathic Pain. J Neurosci 39, 9130–9144. 10.1523/JNEUROSCI.1683-19.2019. [PubMed: 31604834]

66. Huda R, Sipe GO, Breton-Provencher V, Cruz KG, Pho GN, Adam E, Gunter LM, Sullins A, Wickersham IR, and Sur M (2020). Distinct prefrontal top-down circuits differentially modulate sensorimotor behavior. Nat Commun 11, 6007. 10.1038/s41467-020-19772-z. [PubMed: 33243980]

67. Liu X, Chen C, Liu Y, Wang Z, Huang K, Wang F, and Wang L (2018). Gentle Handling Attenuates Innate Defensive Responses to Visual Threats. Front Behav Neurosci 12, 239. 10.3389/fnbeh.2018.00239. [PubMed: 30405368]

68. Zhou Z, Liu X, Chen S, Zhang Z, Liu Y, Montardy Q, Tang Y, Wei P, Liu N, Li L, et al. (2019). A VTA GABAergic Neural Circuit Mediates Visually Evoked Innate Defensive Responses. Neuron 103, 473–488 e476. 10.1016/j.neuron.2019.05.027. [PubMed: 31202540]

69. Evans DA, Stempel AV, Vale R, and Branco T (2019). Cognitive Control of Escape Behaviour. Trends Cogn Sci 23, 334–348. 10.1016/j.tics.2019.01.012. [PubMed: 30852123]

70. Etkin A, and Wager TD (2007). Functional neuroimaging of anxiety: a meta-analysis of emotional processing in PTSD, social anxiety disorder, and specific phobia. Am J Psychiatry 164, 1476–1488. 10.1176/appi.ajp.2007.07030504. [PubMed: 17898336]

71. Ghosh KK, Burns LD, Cocker ED, Nimmerjahn A, Ziv Y, Gamal AE, and Schnitzer MJ (2011). Miniaturized integration of a fluorescence microscope. Nat Methods 8, 871–878. 10.1038/nmeth.1694. [PubMed: 21909102]

72. Resendez SL, Jennings JH, Ung RL, Namboodiri VM, Zhou ZC, Otis JM, Nomura H, McHenry JA, Kosyk O, and Stuber GD (2016). Visualization of cortical, subcortical and deep brain neural circuit dynamics during naturalistic mammalian behavior with head-mounted microscopes and chronically implanted lenses. Nat Protoc 11, 566–597. 10.1038/nprot.2016.021. [PubMed: 26914316]

73. Liang F, Li H, Chou XL, Zhou M, Zhang NK, Xiao Z, Zhang KK, Tao HW, and Zhang LI (2019). Sparse Representation in Awake Auditory Cortex: Cell-type Dependence, Synaptic Mechanisms, Developmental Emergence, and Modulation. Cereb Cortex 29, 3796–3812. 10.1093/cercor/bhy260. [PubMed: 30307493]

74. Zhang GW, Shen L, Tao C, Jung AH, Peng B, Li Z, Zhang LI, and Tao HW (2021). Medial preoptic area antagonistically mediates stress-induced anxiety and parental behavior. Nat Neurosci 24, 516–528. 10.1038/s41593-020-00784-3. [PubMed: 33526942]

75. Harvey CD, Coen P, and Tank DW (2012). Choice-specific sequences in parietal cortex during a virtual-navigation decision task. Nature 484, 62–68. 10.1038/nature10918. [PubMed: 22419153]

76. Wang D, Yeung DS, and Tsang EC (2007). Weighted mahalanobis distance kernels for support vector machines. IEEE Trans Neural Netw 18, 1453–1462. 10.1109/tnn.2007.895909. [PubMed: 18220193]

77. Li H, Wang J, Liu G, Xu J, Huang W, Song C, Wang D, Tao HW, Zhang LI, and Liang F (2021). Phasic Off responses of auditory cortex underlie perception of sound duration. Cell Rep 35, 109003. 10.1016/j.celrep.2021.109003. [PubMed: 33882311]

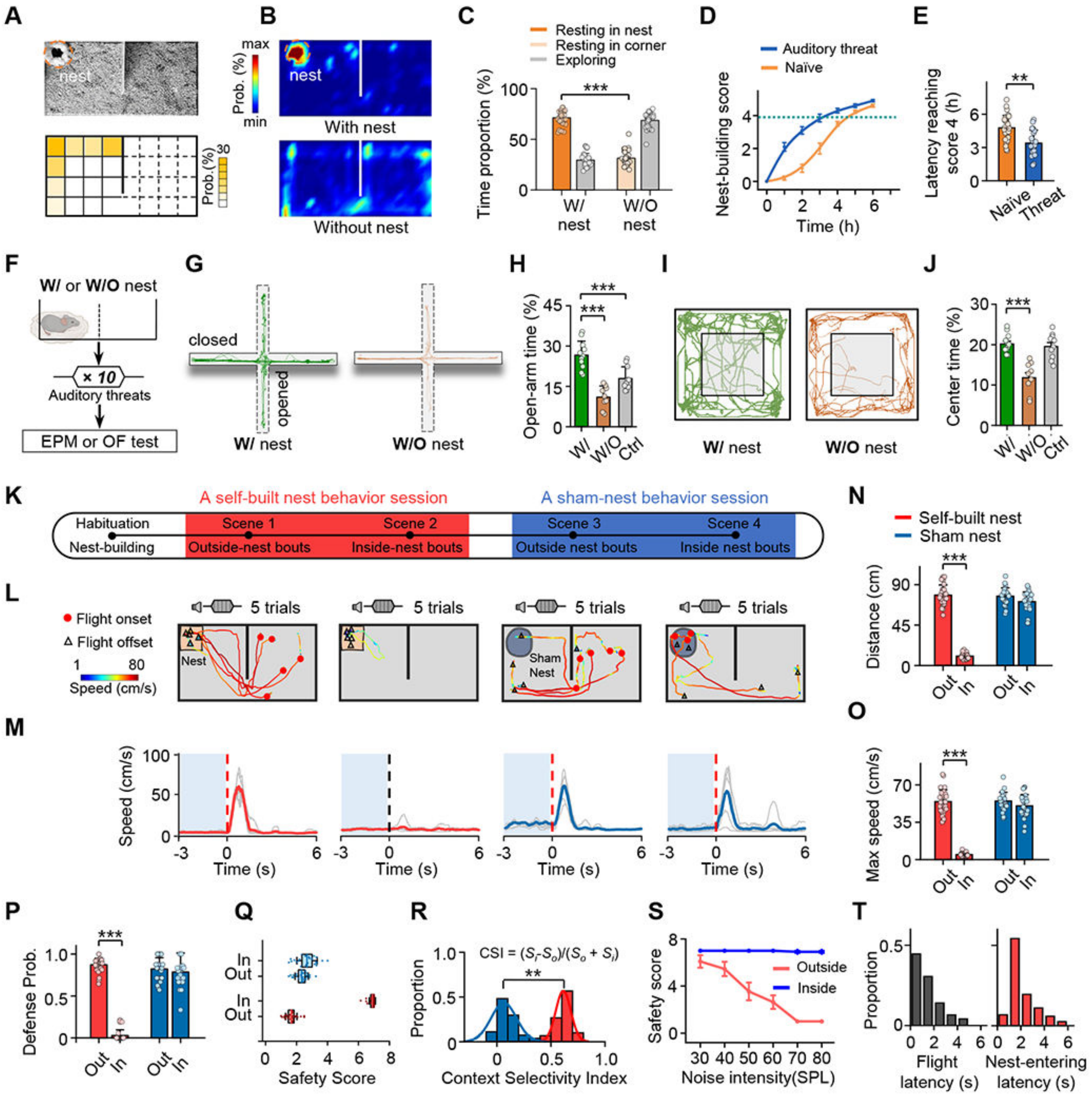

**Figure 1.**

Context-dependent fear responses upon auditory threats.

(A) Top, an example video frame showing the location of the self-built nest. Bottom, distribution of nest locations in the behavior arena. Mirror image was used if the location was on the right side.

(B) Heat map showing distribution of time in different locations of the arena with (top) or without (bottom) the self-built nest for an example mouse.

(C) Comparison of proportions of time staying in the nest (with the self-built nest present) and in a corner (with the nest absent). Grey, time outside the nest (with nest) or in the open area (without nest). Unpaired t test (***P < 0.001, t = 21, n = 30 mice each).

(D) Curve showing nest-building time for naïve mice (orange) and mice that had experienced auditory threats (blue).

(E) Comparison of the nest-building time reaching nest-building score 4 between for naïve mice (orange) and mice that had experienced auditory threats (blue). Unpaired t test (***P < 0.001, t = 4.15, n = 30, 20 mice for Naïve and auditory threat respectively).

(F) Experimental condition: a mouse staying in the arena with or without a self-built nest was exposed to auditory threat signals and after that was subjected to EPM and OF tests.

(G) Movements tracks for an example animal of with- and without-nest conditions in EPM test.

(H) Percentage of time spent in open arms of EPM. Unpaired t test (w/ nest vs. white control: t = 4.1, ***P < 0.001; w/ nest vs. w/o nest: t = 7.26, ***P < 0.001, n = 11, 9, 10 mice for w/ nest group, w/o nest group and white control group respectively).

(I) Movements tracks for example animals in OF test.

(J) Percentage of time spent in center of OF. Unpaired t test (w/ nest vs. w/o nest: t = 6.07, P < 0.001, n = 11, 9, 10 mice for w/ nest group, w/o nest group and white control group respectively).

(K) Schematic of experimental design. After habituation and nest-building, a self-built nest behavioral session under two scenarios (scene 1, noise stimulation was applied when the mouse was outside the self-built nest; scene 2, noise stimulation was applied when it was inside the nest) including 5–8 outside- and 5–8 inside-nest bouts were performed in a randomized order. Following that, in a subset of mice, a sham-nest behavioral session under two scenarios (scene 3 and scene 4) was also performed, similar to the self-built nest behavioral session.

(L) Trajectory with speed plot for an example mouse in each scenario (5 trials). Red dot, location at the onset of flight. Open triangle, location at the end of flight.

(M) Corresponding speed traces of single trials (light grey) and the mean (solid color) for the same mouse shown in (L), aligned to the onset of flight (red dotted line) or noise stimulation (black dotted line). Note that auditory threat was applied only if the mouse had remained relatively quiet for at least 3 seconds (shaded blue).

(N-P) Quantification of the total flight distance (N), maximum speed (O) and defense probability (P) in different scenarios. One-way ANOVA (***P < 0.001, ***P < 0.001 and ***P < 0.001; F = 369, 229 and 249 for (N), (O) and (P), respectively) and post hoc test, n = 30, 25 mice for self-built nest and sham nest respectively. All error bars represent s.e.m.

(Q) Boxplot of safety scores (see Figure S2 for scoring) in different scenarios. Red, for self-built nest; blue, for sham nest.

(R) Distribution of context selectivity indices (CSIs) for the self-built nest group (red) and sham nest group (blue). Kolmogorov-Smirnov test (***P < 0.001, D = 1.00), n = 30, 25 mice for self-built nest and sham nest respectively.

(S) Mean safety score plotted as a function of sound intensity for inside- (blue) and outside-nest (red) bouts, respectively.

(T) Distribution of onset latencies of flight (time from the noise onset to the flight onset, left) and latencies of nest-entering (time from the flight onset to the timing of nest-entering, right).

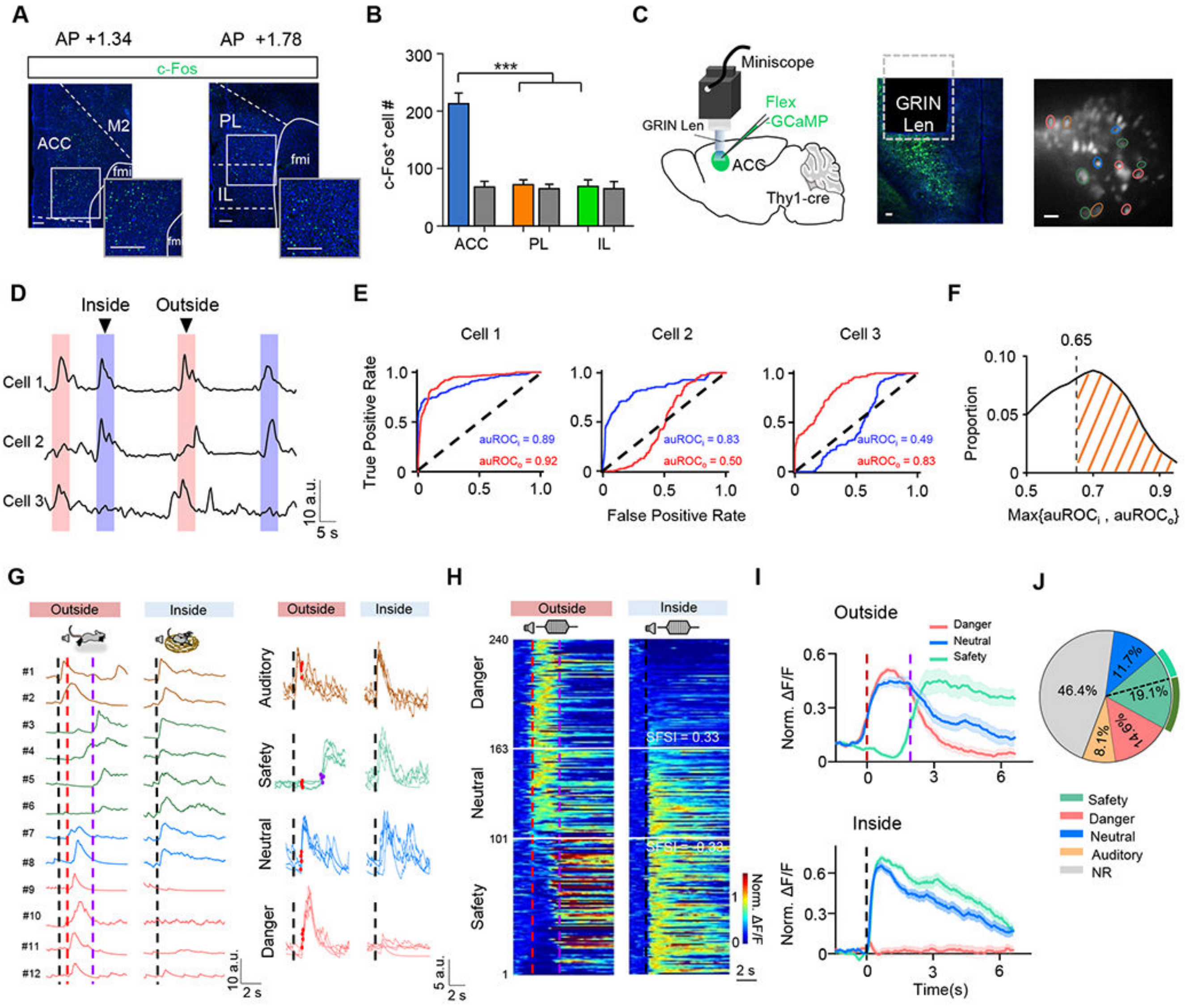

**Figure 2.**

Distinct danger- and safety-related neural representations in ACC.

(A) Image showing c-Fos staining in ACC (left), PL and IL (right) after inside-nest bouts. Blue, DAPI staining. Scale bar, 100 μm.

(B) Comparison of total numbers of c-Fos+ neurons among ACC, PL and IL. Kruskal-Wallis test (***$P < 0.001$, $H = 19.50$), $n = 9$ brain slices from 3 mice. Colored, experiment; gray, control.

(C) Schematic of micro-endoscopic calcium imaging (first panel) in ACC and an example confocal image showing GCaMP7s expression in deep layers of ACC (second panel). An example field of view (FOV) of GCaMP7s-expressing neurons (third panel). Scale bar, 100 μm.

(D) Three example cells showing different activation patterns in outside- and/or inside-nest bouts.

(E) The auROC of the example cells shown in (D) in outside- (red) and inside-nest (blue) bouts, respectively.

(F) Distribution of the largest auROC between outside- and inside-nest bouts for all individual cells. The dashed line indicates the auROC threshold (0.65) for defining event-related neurons.

(G) Left, $Ca^{2+}$ signal traces for example auditory- (cell #1-2, brown), safety- (cell #3-6, green) and danger- (cell #9–12, purple) responding, as well as neutral (cell #7–8, blue) cells from the same FOV shown in (C), aligned to the noise onset. Note that a 5-point smoothing calculation was performed on each trace. Dashed black line, noise onset; dashed red line, flight onset; dashed purple line, timing of nest-entering. Right, single-trial $Ca^{2+}$ response traces of example cells for each type. Red dot marks the onset of flight, and purple dot (safety) marks the timing of nest-entering. Note that the signal traces are after interpolation for alignment (see Figure S3E–S3J for details).

(H) Heatmap of normalized $Ca^{2+}$ signal traces for danger-responding, safety-responding and neutral cells in two scenarios, sorted by SFSI (SFSI = (Po −Pi) / (Po + Pi), where Pi and Po were the peak amplitudes of the normalized $Ca^{2+}$ activity during inside- and outside-nest bouts, respectively; also see STAR Methods) and aligned to the flight onset (dashed red line) in outside-nest bouts (left) or noise onset (dashed black line) in inside-nest bouts (right). Horizontal white lines mark the SFSI thresholds for neural classifications.

(I) Average normalized responses of danger-responding (n = 77 cells), safety-responding (n = 101) and neutral (n = 62) cells shown in (E).

(J) Proportions of safety-, danger-, and auditory-responding, neutral as well as non-responding (NR) cells. Dashed black line separates safety-responding population with (63.8%) and without (36.2%) showing nest-entering responses.

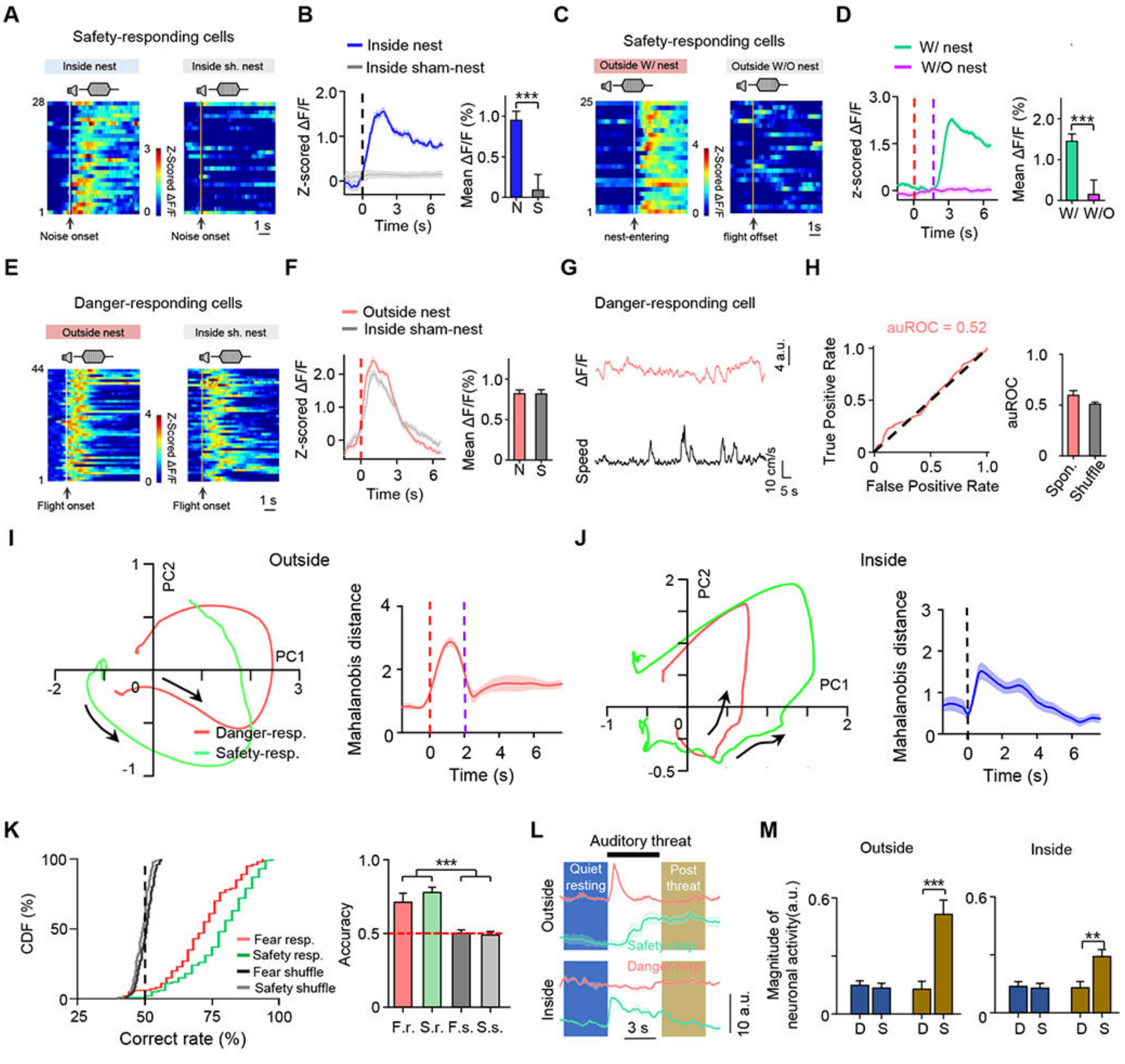

**Figure 3.**

Activity dynamics of danger- and safety-responding neurons under different scenario.

(A) Heatmap for $Ca^{2+}$ responses of a subset of safety-responding cells (with SDSI > 0.5) responding to auditory threats when inside the self-built nest (left) or when inside the sham nest (right).

(B) The average response trace for data shown in (A). Insert, mean ΔF/F during 0–5 sec after noise onset. Wilcoxon signed-rank test (W = 328, $^{***}P < 0.001$, n = 28 cells).

(C) Heatmap of $Ca^{2+}$ responses of a subset of safety-responding cells (with SFSI > 0.5) responding to nest-entering (left) in outside-nest bouts and to flight offset in inside-sham-nest bouts (right).

(D) Average responses for the data shown in (C). Insert, mean ΔF/F during 0–5 sec after nest-entering or flight offset. Wilcoxon signed-rank test (***P < 0.001, W = 325.00), n = 25 cells.

(E - F) Similar to (A-B), but for a subset of danger-responding cells (with SDSI < −0.5) in outside-nest bouts and inside sham-nest bouts. Red dash line marks flight onset. Paired t test (P = 0.215, t =1.258, n = 44 cells).

(G) Spontaneous $Ca^{2+}$ activity trace of an example danger-responding cell (top) and the synchronous running speed (bottom) from a mouse.

(H) The auROC of the example cell (left) shown in (G) and the summary of population cells (right) showing $Ca^{2+}$ activity is not related to locomotion speed of the mouse.

(I - J) Population activity trajectories during behavior projected onto the first two principal components for danger- and safety-responding cells from an example section in outside-nest (I, left) and inside-nest (J, left) bouts, with the average Mahalanobis distance between the two cell populations plotted (I and J, right).

(K) Left, cumulative distribution of decoding accuracy of SVM decoder trained to discriminate different behaviors in two scenarios using the population activity of danger-responding (red) or safety-responding (green) cells. Grey traces are for shuffled data. Right, overall accuracy. One-way ANOVA (***P < 0.001, F = 271.4).

(L) Average $Ca^{2+}$ signal trace of an example safety- (green) and danger-responding (pink) cell in outside- and inside-nest bouts. Shaded boxes denote the analysis time windows in quiet-resting and post-threat periods, respectively.

(M) Comparison of activity levels during quiet-resting (blue) and post-threat (brown) periods between danger-responding ("D") and safety-responding ("S") cells in outside-nest (left) and inside-nest (right) conditions. Unpaired t test (Outside nest: quiet resting, D vs. S, P = 0.427, t = 0.796; post threat, D vs. S, ** * P < 0.001, t = 4.22. Inside nest: quiet resting, D vs. S, P = 0.208, t = 1.263; post threat, D vs. S, **P = 0.002, t = 3.229. n = 77, 101 for danger- and safety-responding cells respectively).

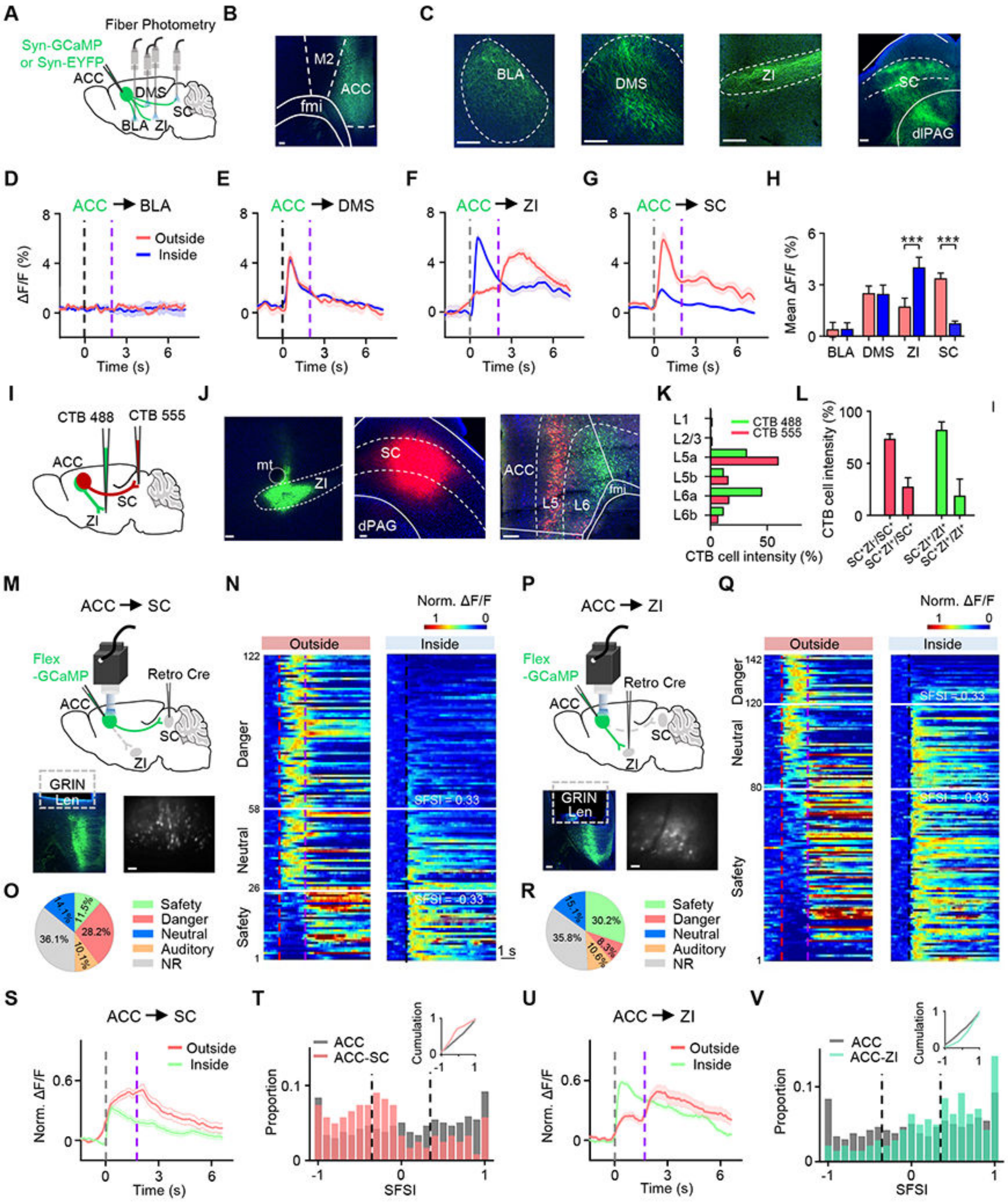

**Figure 4.**

Differential target preferences of safety- and fear-preferring ACC neurons.

(A) Schematic of virus injection and fiber photometry recording of ACC axon terminals in different target areas.

(B) Confocal image showing GFP expression at the injection site. M2, secondary motor cortex.

(C) GFP-labeled ACC axons in different target areas. BLA, basolateral amygdala; ZI, zona incerta; DMS, dorsomedial striatum; dlPAG, dorsolateral periaqueductal gray.

(D-G) Average $Ca^{2+}$ responses of ACC axon terminals in BLA (D), DMS (E), ZI (F) and SC (G), aligned to the flight onset (outside-nest bouts) or noise onset (inside-nest bouts). Note that the traces between two dashed lines in outside-nest bouts were interpolated before averaging.

(H) Mean $\Delta F/F$ during 0–2s after the flight onset (outside-nest bouts) or noise onset (inside-nest bouts). Mann-Whitney test ($P = 0.647$, $P = 0.737$, ***$P < 0.001$ and ***$P < 0.001$; $U = 94$, 129, 0 and 144; $n = 14$, 15, 17, 12 trials for BLA, DMS, ZI and SC respectively).

(I) Schematic of double retrograde labeling with CTB-488 injection in ZI (green) and CTB-555 injection in SC (red).

(J) Confocal images showing CTB expression at injection sites (left and middle) and the retrogradely labeled neurons in ACC (right). Scale bar, 100 μm.

(K) Relative density of neurons retrogradely labeled from ZI (green) and SC (red) at different laminar locations of ACC.

(L) Quantification of single- and double-labeled neurons in ACC.

(M) Top, schematic of micro-endoscopic calcium imaging of SC-projecting ACC neurons. Bottom, example image showing GCaMP7s expression in ACC (left) and a FOV at the imaged site (right). Scale bar, 100 μm.

(N) Heatmap for normalized $Ca^{2+}$ responses separated into safety- and fear-preferring cells in outside-nest (left) and inside-nest (right) conditions.

(O) Pie chart showing proportions of different cell types.

(P-R) Similar to (M-O), but for ZI-projecting ACC neurons.

(S) Average responses for cells ($n = 122$) shown in (N).

(T) Distribution of SFSIs for the overall ACC population and the SC-projecting population. Insert, cumulative distribution. Kolmogorov-Smirnov test (***$P < 0.001$, $D = 0.313$, $n = 240$, 122 for overall and SC-projecting ACC cells respectively).

(U-V) similar to (S-T), but for ZI-projecting neurons. Kolmogorov-Smirnov test (*$P = 0.010$, $D = 0.172$, $n = 240$, 142 for overall and ZI-projecting ACC cells respectively).

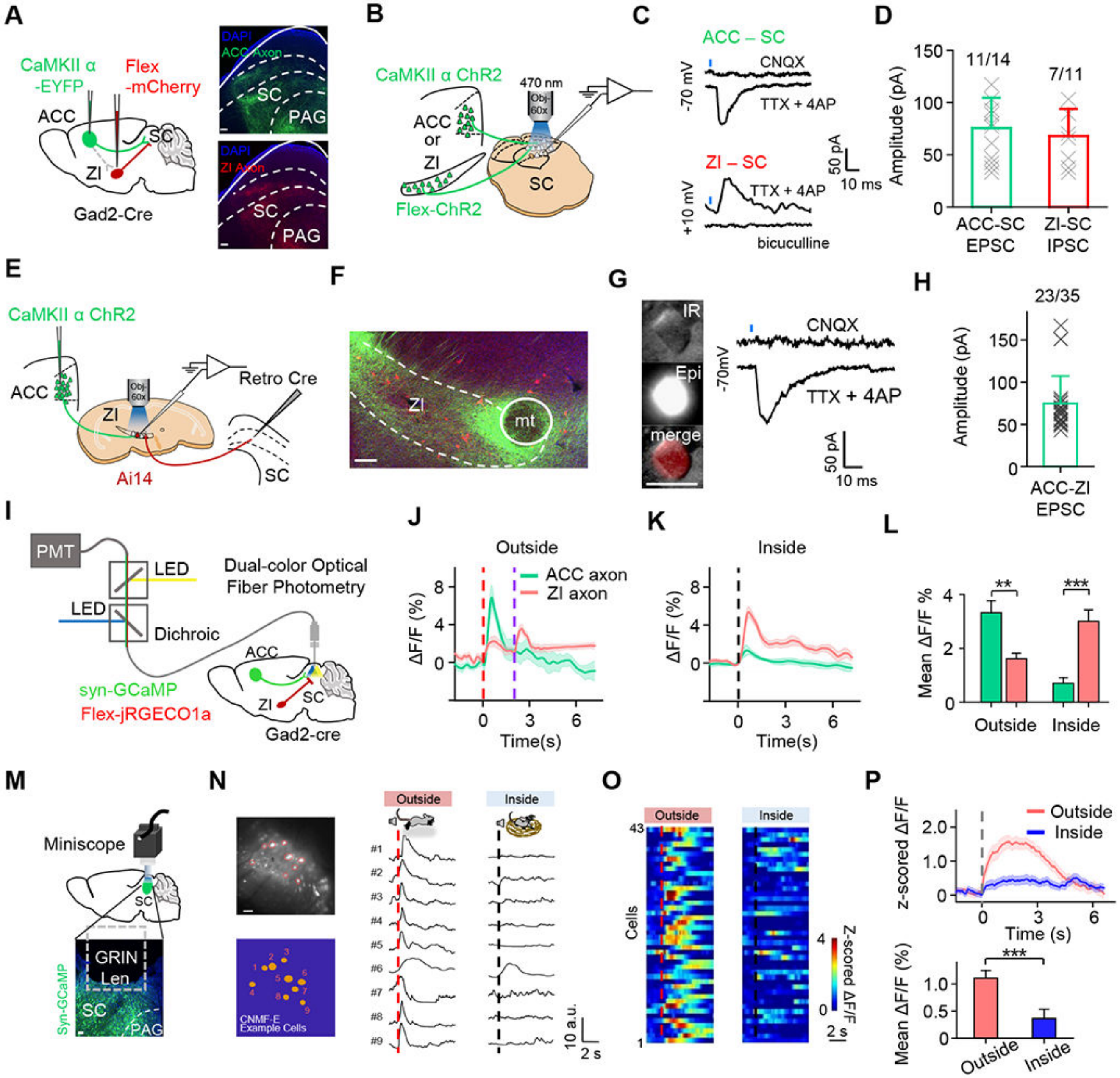

**Figure 5.**

Direct and indirect ACC corticofugal pathways to modulate SC.

(A) Viral injections of CaMKIIα-eYFP and Flex-mCherry injection in ACC and ZI, respectively, in a Gad2-Cre mouse (left). Confocal image (right) shows highly overlapping red-labelled ZI axons and green-labeled ACC axons in SC. Scale bar, 100 μm.

(B) Schematic of whole-cell recording from SC neurons with photoactivation of ACC glutamatergic axons or ZI GABAergic axons in a slice preparation.

(C) A representative light-evoked monosynaptic excitatory postsynaptic current (EPSC) by photoactivating ACC-SC axons (top) and inhibitory postsynaptic current (IPSC) by photoactivating ZI-SC axons (bottom) recorded in SC neurons. A blue tick marks the onset of LED illumination. Note that EPSCs and IPSCs were recorded by clamping the cells at different potentials.

(D) Peak amplitudes of light-evoked monosynaptic ACC-SC EPSCs and ZI-SC IPSCs recorded in SC neurons. Insert, fraction of cells exhibiting evoked responses.

(E) Schematic of recording from retrogradely labeled SC-projecting ZI neurons with photoactivation of ACC glutamatergic axons.

(F) Confocal image showing fluorescence-labeled ACC glutamatergic axons (green) and SC-projecting neurons (red) in ZI. Scale bar, 100 μm.

(G) Left, an example SC-projecting ZI neuron (CTB-positive) being recorded under infrared (IR) and epifluorescence (Epi) imaging. Scale bar, 10 μm. Right, representative light-evoked monosynaptic EPSC.

(H) Peak amplitudes of light-evoked monosynaptic ACC-ZI EPSCs.

(I) Schematic of dual-color fiber photometry recording of $Ca^{2+}$ signals from ACC-SC and ZI-SC axon terminals.

(J-K) Average $Ca^{2+}$ responses of ACC (green) and ZI (red) axon terminals in an example mouse in outside-nest (J) and inside-nest (K) conditions, aligned to the flight onset (outside-nest) or noise onset (inside-nest).

(L) Mean $\Delta F/F$ during 0–2s after the flight onset (outside-nest) or noise onset (inside-nest). Paired t test (outside: $^{**}P = 0.009$, $t = 3.04$, $n = 14$ trials; inside: $^{***}P < 0.001$, $t = 4.52$, $n = 14$ trials).

(M) Schematic of micro-endoscopic calcium imaging of SC neurons (top), and an example image showing GCaMP7s expression in SC (bottom). Scale bar, 100 μm.

(N) Left, an example FOV of GCaMP7s-expressing neurons (top) and cell mask (bottom). Right, $Ca^{2+}$ response traces of nine neurons under two scenarios in a single-trial, aligned to the flight onset (outside-nest) or noise onset (inside-nest).

(O) Heatmap of average $Ca^{2+}$ responses of single SC neurons in outside-nest (left) and inside-nest (right) conditions, aligned to the flight onset (left) or noise onset (right).

(P) Average responses (top) and mean $\Delta F/F$ during 0–5 sec after the flight onset or noise onset (bottom) from SC cells. Paired t test ($^{***}P < 0.001$, $t = 19.88$, $n = 43$ cells).

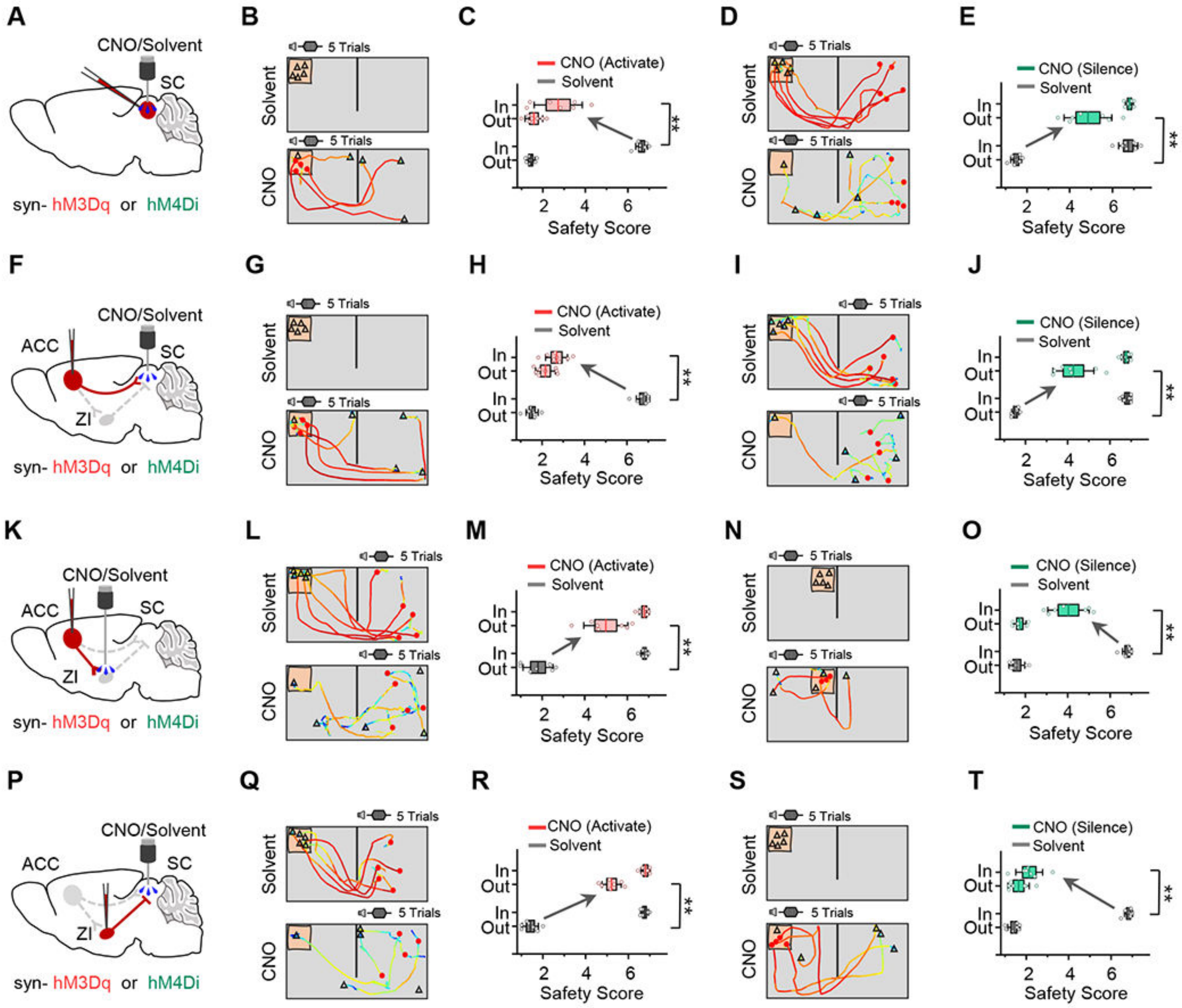

**Figure 6.**

Context-dependent antagonistic modulations of fear response by ACC-SC and ACC-ZI-SC pathways.

(A) Schematic of chemogenetic activation (hM3Dq) or inhibition (hM4Di) of SC neurons.

(B) Trajectory-speed map for an example mouse in the inside-nest condition with solvent (top) or CNO (bottom) infused in SC.

(C) Comparison of safety scores under two scenarios between solvent and CNO applications. Wilcoxon signed rank test (**P = 0.009, W = 28, n = 7 mice).

(D-E) Similar to (B-C), but for chemogenetic inhibition of SC neurons in a mouse in the outside-nest condition. Wilcoxon signed rank test (**P = 0.009, W= 28, n = 7 mice).

(F-J) Similar to (A-E), but for chemogenetic activation (G-H) or inhibition (I-J) of ACC axon terminals in SC. For (H), Wilcoxon signed rank test (**P = 0.004, W = 36, n = 8 mice); for (J), Wilcoxon signed rank test (**P = 0.009, W = 28, n = 7 mice).

(K-O) Similar to (A-E), but for chemogenetic activation (L-M) or inhibition (N-O) of ACC axons in ZI. For (M), Wilcoxon signed rank test (**P = 0.009, W = 28, n = 7 mice); for (O), Wilcoxon signed rank test (**P = 0.009, W = 28, n = 7 mice).

(P-T) Similar to (A-E), but for chemogenetic activation (Q-R) or inhibition (S-T) of ZI GABAergic axons in SC. For (R), Wilcoxon signed rank test (**P = 0.009, W = 28, n = 7 mice); for (T), Wilcoxon signed rank test (**P = 0.009, W = 28, n = 7 mice).

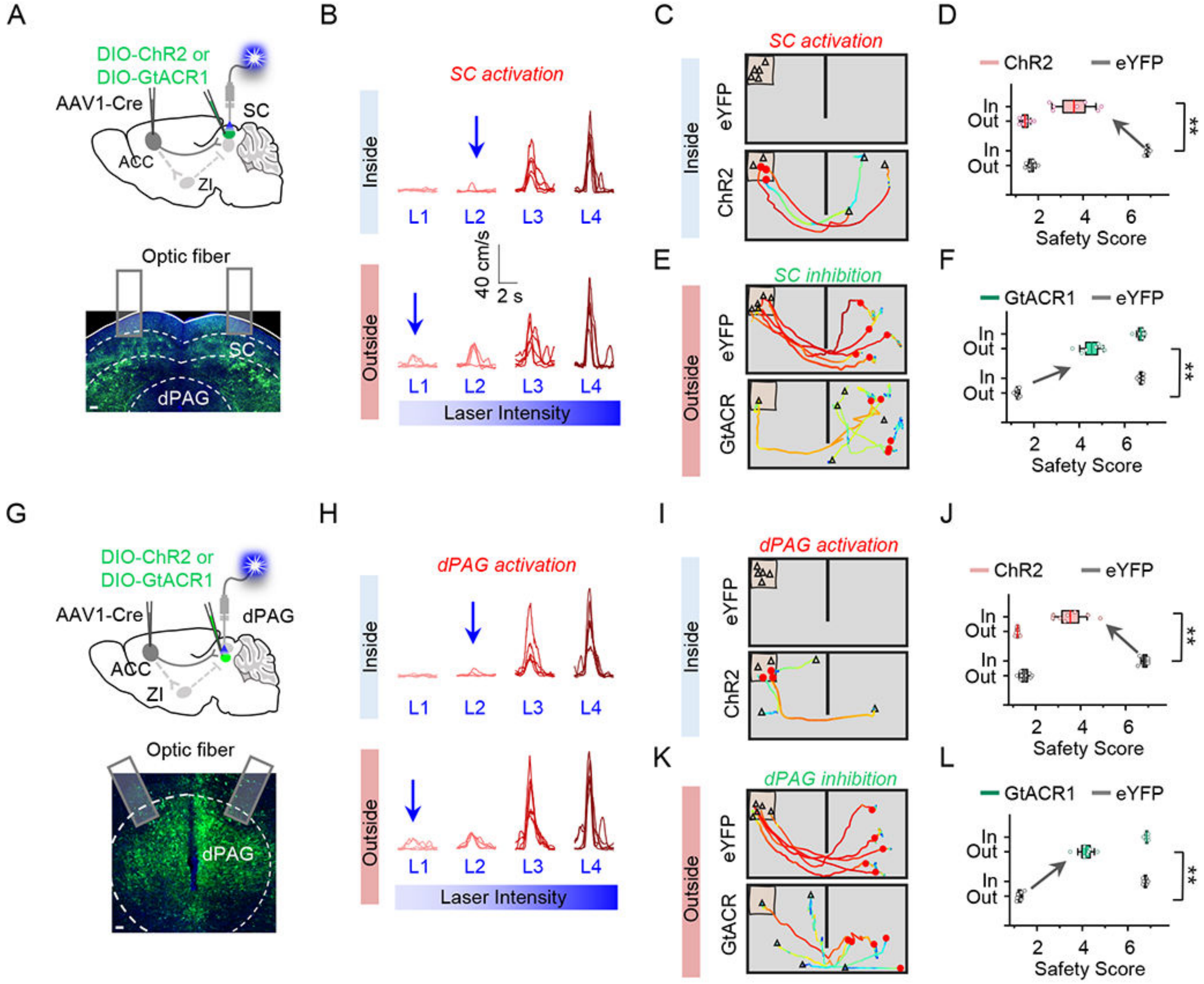

**Figure 7.**

ACC projections to SC and dPAG have similar functional effects.

(A) Top, schematic of viral injection strategy for activation (ChR2) or inhibition (GtACR1) of ACC-recipient neurons in SC. Bottom, image showing the expression of ChR2 in SC. Scale bar, 100 μm.

(B) Speed traces of an example mouse in response to activation of ACC-recipient SC neurons with increasing laser intensities in the inside- (top) or outside-nest (bottom) condition. The blue arrow indicates the intensity of laser used for the optogenetic experiment, which was the maximum intensity that did not elicit flight behavior.

(C) Trajectory-speed map for an example mouse in the inside-nest condition in the eYFP (top) or ChR2 (bottom) group with optogenetic activation.

(D) Comparison of safety scores in two scenarios between eYFP and ChR2 groups. Wilcoxon signed rank test (**P = 0.008, W = 28, n = 7 mice).

(E) Trajectory-speed map for an example mouse in the outside-nest condition in the eYFP (top) or GtACR1 (bottom) group with optogenetic inhibition.

(F) Comparison of safety scores in two scenarios between eYFP and GtACR1 groups. Wilcoxon signed rank test (**P = 0.008, W = 28, n = 7 mice).
(G-L) Similar to (A-F), but for optogenetic activation (I-J) or inhibition (K-L) of ACC-recipient dPAG neurons. For (J), Wilcoxon signed rank test (**P = 0.004, W = 36, n = 8 mice); for (L), Wilcoxon signed rank test (**P = 0.008, W = 28, n = 7 mice).

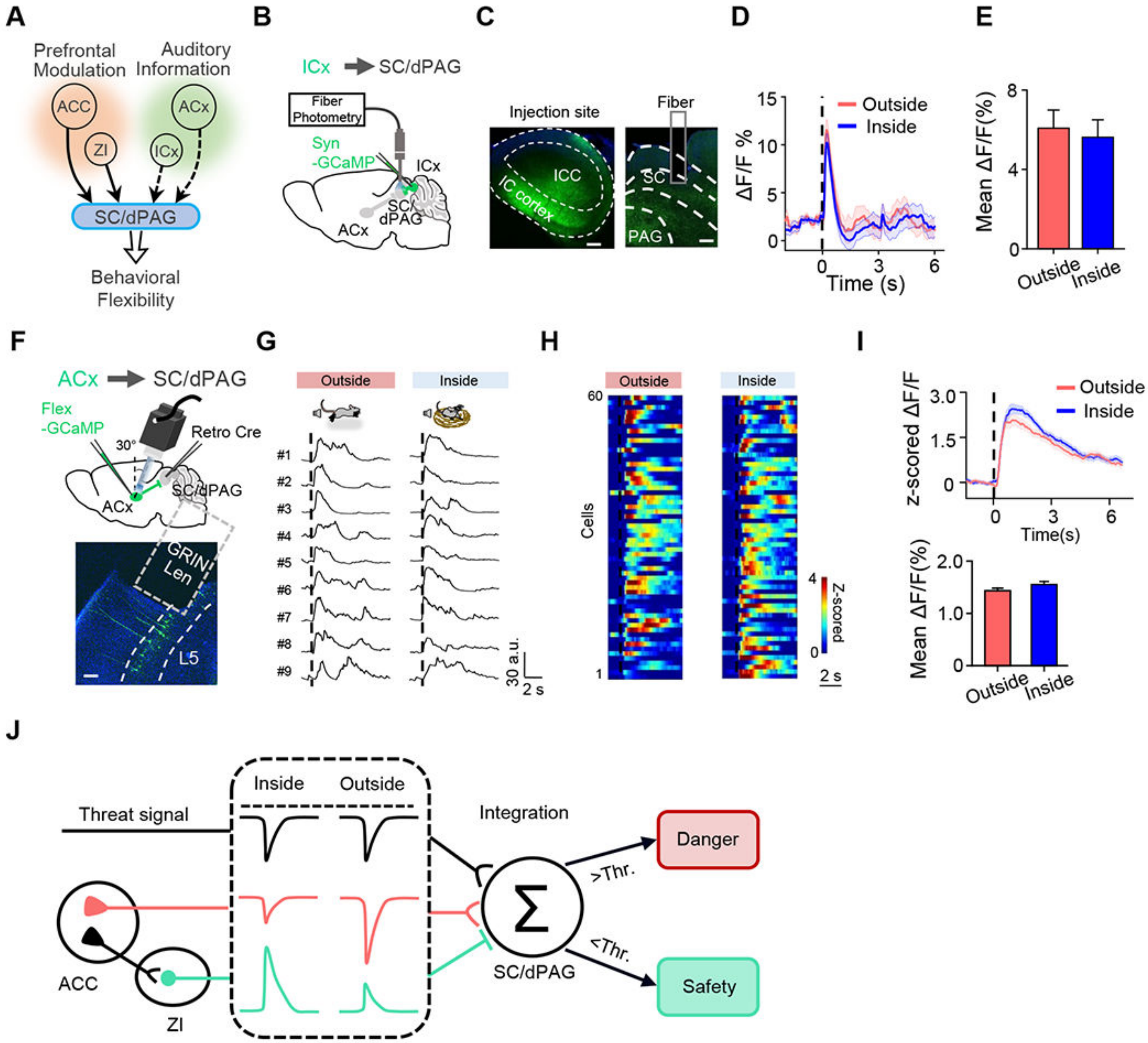

**Figure 8.**

Non-context-dependent auditory signals to SC.

(A) Potential sources of context-dependent signals to SC/dPAG.

(B) Schematic of fiber photometry recording of ICx axons in SC.

(C) Confocal images showing GCaMP7s expression at the injection site (left) and in SC (right).

(D) Average $Ca^{2+}$ response traces under two scenarios for an example mouse.

(E) Mean ΔF/F during 0–1 sec after the noise onset. Mann-Whitney test ($P = 0.900$, $U = 194.00$). n = 18, 21 bouts for outside and inside respectively.

(F) Schematic of micro-endoscopic $Ca^{2+}$ imaging of SC-projecting ACx neurons (top), and confocal image showing GCaMP7s expression in ACx (bottom). Scale bar, 100 μm.

(G) $Ca^{2+}$ response traces of nine neurons in a FOV responding to noise stimulation, aligned to the noise onset (dashed black line).

(H) Heatmap for average $Ca^{2+}$ responses of single ACx neurons in outside-nest (left) and inside-nest (right) conditions.

(I) Average responses (top) and mean ΔF/F during 0–5 sec after the noise onset (bottom). Wilcoxon signed-rank test (P= 0.761, W= 873.00), n = 60 cells.

(J) Schematic illustration of the proposed neural pathways underlying context-dependent flexibility of fear reactions.

## KEY RESOURCES TABLE

| REAGENT or RESOURCE | SOURCE | IDENTIFIER |
|---|---|---|
| **Antibodies** | | |
| Rabbit monoclonal anti-c-fos | Cell Signaling | Cat#2250S |
| Alexa Fluor 488 goat anti-rabbit IgG | Abcam | Cat#ab150077 |
| Mounting Medium, antifading (with DAPI) | Solarbio | Cat#S2110 |
| | | |
| **Bacterial and virus strains** | | |
| AAV2/9-syn-jGCaMP7s-WPRE | OBiO | H11264 |
| AAV2/1-syn-FLEX-jGCaMP7s-WPRE | OBiO | H11256 |
| AAV2/9-hSyn-FLEX-NES-jRGECO1a-WPRE | OBiO | H11158 |
| AAV2-retro-hSyn-Cre | Vigene | AV204006 |
| AAV2/9-hSyn-hM3D(Gq)-mCherry | OBiO | N/A |
| AAV2/1-hSyn-Cre | OBiO | CN867 |
| AAV2/9-EF1α-DIO-eYFP | OBiO | AG20296 |
| AAV2/9-DIO-hChR2 (H134R)-eYFP | OBiO | AG20298 |
| AAV2/9-DIO-GtACR1-eYFP | OBiO | N/A |
| AAV2/9-CaMKIIα-hChR2(H134R)-eYFP | OBiO | AG26969 |
| AAV2/9-syn-FLEX-eYFP | OBiO | N/A |
| AAV2/9-hSyn-GFP | BrainVTA | PT-1990 |
| AAV2/9-EF1α-DIO-mCherry-WPRE-hGH | BrainVTA | PT-0013 |
| | | |
| **Chemicals, peptides, and recombinant proteins** | | |
| NaCl | OmniPur | UI27FZEMS |
| KCl | Mallinckrodt | 7447-40-7 |
| $NaHCO_3$ | EMD Chemicals | 48204847 |
| $MgCl_2$ | J.T. Baker | 7791-18-6 |
| $CaCl_2$ | EMD Chemicals | 41046444 |
| $NaH_2PO_4$ | EMD Chemicals | SX0320-1 |
| Cs-Gluconate | Sigma | G4625 |
| TEA-Cl | Sigma | T2265 |
| CsCl | Sigma | 289329 |
| HEPES | Sigma | SLBX2493 |
| EGTA | Sigma | 324626 |
| GTP | Sigma | G8877 |
| Phosphocreatine | Sigma | P7936 |
| QX-314 | Sigma | L5783 |
| MgATP | Sigma | A9187 |
| Glucose | Sigma | SLBC6575V |
| Sucrose | Sigma | D00168514 |

| REAGENT or RESOURCE | SOURCE | IDENTIFIER |
|---|---|---|
| Biocytin | Sigma | B4261 |
| Agar | BioFroxx | 1182GR500 |
| Paraformaldehyde | Alfa Aesar | 10194340 |
| | | |
| **Experimental models: Organisms/strains** | | |
| Mouse: C57BL/6J | The Jackson Laboratory | RRID: IMSR_JAX:000664 |
| Mouse: Ai14 | The Jackson Laboratory | RRID: IMSR_JAX:007914 |
| Mouse: VGluT2-ires-Cre | The Jackson Laboratory | RRID: IMSR_JAX: 016963 |
| Mouse: GAD2-ires-Cre | The Jackson Laboratory | RRID: IMSR_JAX: 010802 |
| Mouse: Thy1-Cre | The Jackson Laboratory | RRID: IMSR_JAX: 006143 |
| | | |
| **Software and algorithms** | | |
| LabVIEW | LabVIEW | http://www.ni.com; RRID: SCR_014325 |
| Matlab | Matlab | http://www.mathworks.com/; RRID: SCR_001622 |
| Prism | GraphPad | https://www.graphpad.com/scientific-software/prism/; RRID: SCR_00279 |
| Fiji | NIH | https://fiji.sc/; RRID: SCR_002285 |
| Custom codes for analysis | This paper | |
| | | |
| **Other** | | |
| NI board for data acquisition | National Instrument | PCl-6731 |
| Sound-Attenuation Booth | | |
| Free Field Speaker | Tucker-Davis Technologies | TDT ES1 |
| | | |